communications biology

A Nature Portfolio journal

Article

https://doi.org/10.1038/s42003-025-08940-w

N-phenylquinazolin-4-amine-based EGFR TKIs suppress pulmonary fibrosis by modulating the EGFR/ERBB3 axis in epithelial–macrophage interaction

Ji-Hee Kim[1], Seo-Hyun Choi[1], Jae-Kyung Nam[1], Min-sik Park[1], Haeng Ran Seo[2], Inhee Choi[3], Hae-June Lee[1,4], Jaeho Cho[5], Jeeyong Lee[1] & Yoon-Jin Lee[1]

Although EGFR signaling plays a key role in pulmonary fibrosis (PF), its therapeutic targeting remains limited. This study evaluates N-phenylquinazolin-4-amine-based EGFR tyrosine kinase inhibitors (TKIs) in murine models of bleomycin- and radiation-induced PF. These TKIs attenuated fibrosis by modulating the alveolar epithelial EGFR/ERBB3 axis. EGFR ligands (EGF, EREG, NRG1) were upregulated in pro-inflammatory monocyte-derived alveolar macrophages during early inflammation, with sustained EGFR/ERBB3 phosphorylation in epithelial cells. EGFR/ERBB3 knockdown in human alveolar epithelial cells reduced inflammatory cytokines. Dacomitinib more effectively suppressed TNF-α, IFN-γ, and IL-6 than nintedanib, suggesting a feedback loop driving fibrosis. Elevated phosphorylated EGFR/ERBB3 in RIPF and IPF tissues, and EGFR-related gene expression in epithelial cells from IPF single-cell RNA-seq data, further support clinical relevance. These findings highlight the importance of targeting immune–epithelial EGFR/ERBB3 signaling and support EGFR TKIs as a promising antifibrotic strategy.

Pulmonary fibrosis (PF) refers to a group of interstitial lung diseases characterized by fibrotic remodeling, triggered by known environmental, occupational, or therapeutic exposures such as radiation, bleomycin and silica. Idiopathic pulmonary fibrosis (IPF), in contrast, is a chronic and progressive form of PF without a known cause with a poor prognosis; the estimated mean survival time of patients with IPF is 2–5 years from diagnosis[1,2]. Although the etiology of IPF is undefined, the bleomycin-induced fibrosis model is widely used in preclinical research due to its ability to replicate key of human IPF. PF incidence and prevalence are increasing globally[3]. PF results from various processes that cause chronic lung damage due to excessive deposition of extracellular matrix (ECM) components and profibrotic cell proliferation[4], resulting in scarring and irreversible loss of lung function. Transforming growth factor-β (TGF-β), platelet-derived growth factor (PDGF), and fibroblast growth factors (FGF) act as profibrotic mediators in PF pathogenesis[5]. Fibroblasts play an essential role in PF development. Alveolar epithelial cells undergo epithelial–mesenchymal transition (EMT) to become activated myofibroblasts that secrete collagen and ECM proteins[6]. Furthermore, activated macrophages from tissue-resident macrophage and blood monocyte populations activate fibroblasts by secreting profibrotic cytokines. In the fibrotic phase of PF, interactions between activated macrophages and myofibroblasts are thought to contribute to disease progression[6,7].

Research related to PF has made significant progress; however, treatment options remain limited. Two FDA-approved drugs for IPF, nintedanib (Ofev) and pirfenidone (Esbriet), were recently reported to only delay PF progression but not inhibit or reverse it[1]. Therefore, the development of new drugs to overcome the limitations in current treatment options for PF is urgently required.

In patients with thoracic tumors, radiation therapy can lead to radiation-induced pulmonary injury, which is associated with significant morbidity and mortality and can progress to acute radiation pneumonitis (RP) and subsequently to radiation-induced pulmonary fibrosis (RIPF)[8]. To model these clinical phenomena, we employed mouse models of thoracic irradiation, in which various cytokines are produced through a nonspecific

[1]Division of Radiation Biomedical Research, Korea Institute of Radiologic and Medical Sciences, Seoul, Korea. [2]Advanced Biomedical Research Lab, Institut Pasteur Korea, Seongnam-si, Gyeonggi-do, Republic of Korea. [3]Medicinal Chemistry, Institut Pasteur Korea, Seongnam-si, Gyeonggi do, Republic of Korea. [4]College of Veterinary Medicine, Jeju National University, Jeju, Republic of Korea. [5]Department of Radiation Oncology, Yonsei University College of Medicine, Seoul, Republic of Korea. e-mail: yjlee8@kirams.re.kr

acute response—termed a cytokine storm—following lung irradiation. Notably, elevated cytokine levels following irradiation have been observed in both clinical and preclinical settings[8]. Various proinflammatory cytokines, such as IL-6 and TNF-α, affect acute RP[9] and are thus thought to have diagnostic potential for RP; these cytokines contribute to fibrosis by activating fibroblasts and inducing collagen production[10]. Moreover, the levels of proinflammatory cytokines, such as TNF-α and IL-6, also increase following the intratracheal instillation of bleomycin, causing bleomycin-induced pulmonary fibrosis (BIPF)[11–13].

The epidermal growth factor receptor (EGFR) family includes ERBB1 (EGFR/HER1), ERBB2 (HER2), ERBB3 (HER3), and ERBB4 (HER4); these tyrosine kinase receptors bind the epidermal growth factor (EGF) family of ligands, which includes EGF, TGF-α, and other EGF-like ligands. EGFR signaling plays a crucial role in pulmonary epithelial cell proliferation, ciliated cell differentiation, and the maintenance of airway homeostasis. It also influences immune responses by modulating macrophage activation and platelet-mediated antimicrobial functions, and contributes to tissue fibrosis through dendritic cell-derived ligands[14–16]. Among the EGFR tyrosine kinase inhibitors (TKIs), dacomitinib, afatinib, and sapitinib—each with an N-phenylquinazolin-4-amine core—were originally developed as second-generation or pan-HER inhibitors for non-small cell lung cancer (NSCLC). AC480 shares this core but differs in kinase selectivity. In contrast, osimertinib, CO1686, and WZ4002, which lack the core structure, are third-generation TKIs targeting mutant EGFR, especially the T790M resistance mutation[14]. Although these agents are well established in oncology, their efficacy and mechanisms in pulmonary fibrosis remain poorly understood and have not been validated in clinical studies[17,18]. Interestingly, nintedanib also inhibits EGFR activity in lung fibroblasts derived from patients with IPF[17]. EGFR tyrosine kinase inhibitors (TKIs), ranging from first to fourth generation drugs, have been developed as structural approaches to overcome drug resistance to numerous small molecule compounds[18]. However, their effectiveness as therapeutic agents for PF has not been verified in clinical studies. Furthermore, specific mechanisms of drug action regarding their efficacy in controlling PF have been rarely reported.

Macrophage polarization into pro-inflammatory or anti-inflammatory phenotypes is shaped by microenvironmental cues and the subsequent intracellular signaling cascades[19]. Macrophages derived from tissue-resident macrophages or blood monocytes activate fibroblasts by secreting various cytokines during PF[7,20]. Recently, FA-TLR7-54 was reported to reprogram M2-like fibrosis-inducing macrophages to inhibit BIPF by decreasing the release of profibrotic cytokines[19]. In this study, we utilized RIPF and BIPF mouse models to investigate the potential of EGFR inhibitors in pulmonary fibrosis. Specifically, we aimed to determine. Specifically, we aimed to investigate whether EGFR TKIs modulate macrophage polarization and epithelial responses via the EGFR axis to ultimately modulate fibrotic progression.

Results

Increased phosphorylation of EGFR/ERBB3 and single-cell RNA sequencing analysis in lung fibrosis patients

To evaluate the clinical relevance of EGFR signaling in PF, we investigated whether EGFR and ERBB3 activity were increased in tissues from patients with RIPF who underwent radiotherapy for lung cancer ($n = 8$) or from those with IPF ($n = 8$). Consistent with our mouse studies, the phosphorylated EGFR and ERBB3 levels were significantly higher in RIPF ($P < 0.01$) and IPF tissues ($P < 0.001$) than those in normal lung tissues. These proteins were detected in both alveolar epithelial cells and alveolar macrophages (Fig. 1A), particularly in T1α-positive alveolar type I (AT1) and pro-SPC-positive alveolar type II (AT2) epithelial cells, as further confirmed by co-immunofluorescence staining (Fig. 1B). These data indicated that ERBB3 phosphorylation occurs in human RIPF and IPF, suggesting that EGFR inhibitors targeting EGFR and ERBB3 in alveolar cells might be effective against human PF.

To investigate whether EGFR signaling is relevant in human pulmonary fibrosis, we analyzed two independent scRNA sequencing datasets from patients with IPF. The GEO series GSE135893 provides experimental data from 12 IPF and 10 control lungs[21]. We investigated the expression patterns of EGFR-related receptors in epithelial cells from both IPF and control samples. We identified and visualized $Epcam^+$ epithelial cells using UMAP (Fig. 1C). We found that the number of ERBB2/3/4-positive epithelial cells and the expression levels of EGFR and ERBB2/3/4 were higher in IPF lungs compared with those in control lungs (Fig. 1C). Furthermore, we observed an increase in both the number of gene-positive cells and the expression of EGF-related ligands, including EGF and EREG, in the epithelial cells of IPF patients compared with those in normal lung tissues (Fig. 1C, bottom).

Moreover, we reanalyzed the IPF single-cell data published by Adams et al.[22] identifying lung samples from 32 patients with IPF and 28 control individuals (Fig. S1A). Based on the selected EGF-responsive genes[23], *JUN, FOS, DUSP1, ZFP36, S100A10, S100A6*, and *S100A4* exhibited significantly elevated expression levels in patients with IPF compared with those in the control group. Notably, we observed a substantial increase specifically in myeloid cells and macrophages (Fig. S1A). Gene Ontology analysis of the EGFR signaling pathway[23] revealed the increased expression of pathway-associated genes in fibroblasts and basal cells from patients with IPF, compared with that in the control group. Additionally, aberrant basal cell types showed significant upregulation of the expression of EGFR-related genes, including *AREG, EGF, HER3*, and *PTPN12*, compared with that in basal cells and control (Fig. S1B). Nava et al.[23] termed these cells, which coexpress basal epithelial, mesenchymal, senescent, and developmental markers, aberrant basaloid cells. These findings provided support for the involvement of EGF-responsive myeloid cells, macrophages, and EGFR/ERBB3-regulated epithelial cells in PF pathogenesis.

EGFR TKIs with an N-phenylquinazolin-4-amine core structure effectively inhibit RIPF

Hyperactive EGFR signaling is implicated in epithelial cell proliferation and collagen deposition in PF; thus, we evaluated the regulatory effect of several EGFR TKIs on RIPF. The RIPF mouse model is suitable for observing the efficacy of antifibrotic agents, as it demonstrates the extent of fibrosis in relation to the dose and volume of radiation[24,25].

A single radiation dose of 90 Gy was delivered to the left lung of mice with a 4 mm collimator to induce RIPF[25–27]. EGFR inhibitor dosing was determined based on previously reported effective and well-tolerated concentrations in lung and other solid tumor models[28–31]. Body weight monitoring under the RIPF treatment conditions showed that dacomitinib induced a slight decrease in body weight by day 4, followed by recovery, indicating overall tolerability of the drug (Fig. S2A). After 14 d, RIPF progression was evaluated using the Ashcroft score, an indicator of fibrosis, and trichrome staining, a marker of collagen deposition (Fig. 2A). Interestingly, compared with the vehicle, the EGFR inhibitors sapitinib, afatinib, and dacomitinib, which have an N-phenylquinazolin-4-amine core structure (Table 1), effectively inhibited RIPF, as evidenced by the lower Ashcroft score and smaller trichrome-positive area (Fig. 2A). However, AC480, which has a similar core structure, did not significantly inhibit RIPF. Osimertinib showed modest inhibition of RIPF, although less pronounced than that observed with sapitinib, afatinib and dacomitinib, CO1686 and WZ4002, which do not have an N-phenylquinazolin-4-amine structure, also did not inhibit RIPF (Fig. 2A).

To assess the differential effects of EGFR inhibitors in vitro, we treated human primary pulmonary alveolar epithelial cells (HPAEps) with these inhibitors and performed immunoblotting to detect the activity of EGFR, ERBB2, ERBB3, and ERBB4 based on their phosphorylation levels (Fig. 2B). To confirm band specificity, we additionally performed siRNA-mediated knockdown of each EGFR family member (Fig. S2C). In HPAEps, EGFR phosphorylation increased 1.2–1.83-fold after EGF or epiregulin (EREG) treatment, whereas neuregulin (NRG) treatment slightly increased ERBB3 phosphorylation. Interestingly, similar to their inhibitory effects on RIPF, sapitinib, afatinib, and dacomitinib completely inhibited the phosphorylation of EGFR and ERBB3 but not that of ERBB2 and ERBB4. AC480,

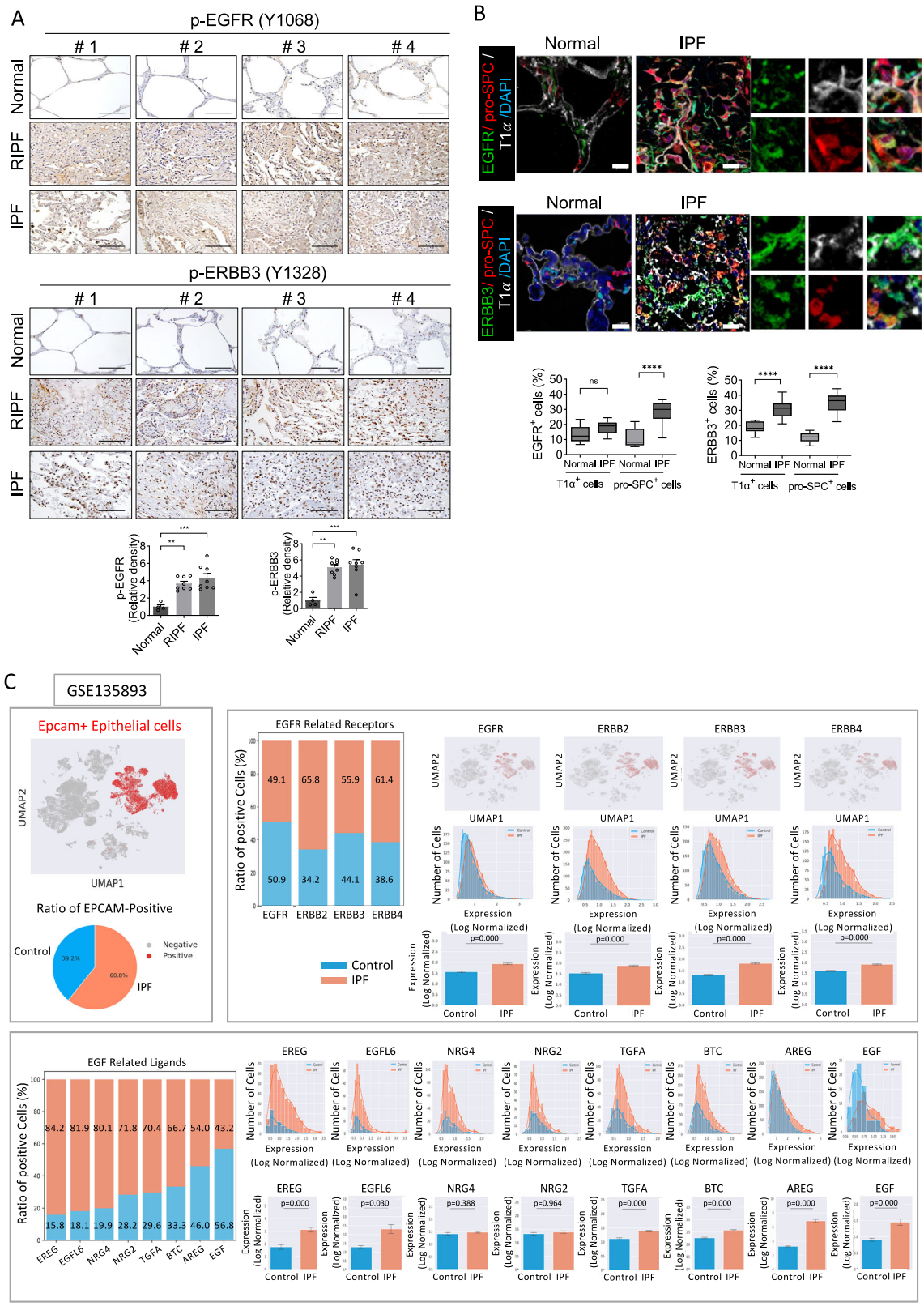

osimertinib, CO1686, and WZ4002 did not decrease EGFR, ERBB2, ERBB3, or ERBB4 phosphorylation in HPAEps (Fig. 2B and Fig. S2B). Additionally, other EGFR TKIs with an N-phenylquinazolin-4-amine core structure, including lapatinib, gefitinib, and BDTX-189, effectively inhibited EGFR and ERBB3 phosphorylation in HPAEps. Conversely, as expected, EGFR TKIs without the core structure, including avitinib, EGFR inhibitor, and AG18, did not inhibit EGFR or ERBB3 phosphorylation in HPAEps (Fig. S3).

Next, we explored the regulatory signaling pathway associated with the inhibitory effects of EGFR or ERBB3 in HPAEps. Interestingly, we observed a consistent trend of inhibitory effects on STAT5 phosphorylation, rather than on the well-known downstream target of EGFR, STAT3 (Fig. S4A).

Fig. 1 | Increased EGFR/ERBB3 phosphorylation and single-cell RNA sequencing analysis in lung tissues from patients with PF. A Immunohistochemistry staining of p-EGFR and p-ERBB3 in lung tissues from IPF ($n = 8$), RIPF ($n = 8$), and healthy ($n = 4$) samples. Scale bar = 20 μm. The average of five fields of p-EGFR and p-ERBB3 density was quantified (magnification: 200×). **B** Immunofluorescence staining of EGFR (green), ERBB3 (green), pro-SPC (red), and T1α (white) was performed on lung tissues from IPF, and healthy samples; scale bar = 20 μm; The average of five fields of EGFR and ERBB3 positive cells was quantified (magnification: 200×). **C** Single cell RNA sequencing data of patients with IPF (GSE135893) were downloaded from the Gene Expression Omnibus (GEO) public repository. The downloaded data were processed as described in "Methods". The specific marker (EPCAM) was used for epithelial cell type assignment. The assigned cells were visualized using the UMAP plotting function, with the ratio of two categories (control and IPF) being shown in pie chart. The expression pattern of EGF-related ligands in epithelial cells are shown. The expression pattern of EGFR-related receptors in epithelial cells are shown. The ratios of categories (control and IPF) in the indicated gene-positive epithelial cells are shown. The expression levels of EGF-downstream genes in epithelial cells are shown. Scanpy core plotting functions and seaborn package (version 0.12.2) were used for graphical presentation. Error bars indicate standard errors. *P*-values (Mann-Whitney U test) are denoted in the bar-graphs. Statistical significance was determined by one-way ANOVA with multiple comparisons ($^{*}P < 0.05$, $^{**}P < 0.01$, $^{***}P < 0.001$, $^{****}P < 0.0001$; ns, not significant).

To investigate the mechanism by which EGFR inhibition affects STAT5 phosphorylation independently of STAT3, we performed siRNA-mediated knockdown of EGFR and ERBB3 in human alveolar epithelial cells (Fig. S4B). Knockdown of EGFR (*EGFR1* siRNA), ERBB3 (*EGFR3* siRNA), or both (*EGFR1* + *3* siRNA) led to a clear reduction in phosphorylated STAT5 levels. In contrast, phosphorylated STAT3 and p-ERK levels were only slightly reduced under EGFR1 knockdown and remained largely unchanged in other conditions. These results suggest that EGFR-mediated STAT5 activation occurs through a STAT3-independent mechanism. Compared to si-Control irradiated cells, siRNA-mediated STAT5 knockdown in HPAEps effectively suppressed radiation-induced fibrotic changes, as indicated by reduced FSP1 (fibroblastic marker) expression and phalloidin (actin cytoskeleton) intensity (Fig. S4C). These findings support the involvement of STAT5 in EGFR-mediated fibrotic responses; however, further studies are needed to clarify the underlying mechanisms.

EGFR TKIs with an N-phenylquinazolin-4-amine core structure inhibited alveolar epithelial EGFR and ERBB3 phosphorylation, in alignment with the mitigating effects of RIPF in vivo. Based on these findings, we propose the potential development of clinically available EGFR TKIs as RIPF inhibitors.

N-phenylquinazolin-4-amine core structure-based EGFR inhibitors mitigate RIPF by modulating the EGFR/ERBB3 axis in alveolar epithelial cells

Next, we investigated the microenvironment of the activation of the EGFR-axis signaling during mouse RIPF development in vivo. RNA sequencing (RNA-seq) analysis (deposited in the GEO repository, GSE306230) conducted on selectively sampled lung tissues exclusively from irradiated areas revealed significant alterations in various ECM components during the 8 to 14-d period postirradiation (Fig. S5). Notably, there was upregulation of metalloproteinases (*Mmp2*, *Mmp12*, *Mmp14*) and collagen genes—both key drivers of fibrotic ECM remodeling— as well as downregulation of decorin (*Dcn*), a known inhibitor of TGF-b signaling (Fig. 3A, Fig. S5). These findings suggest that active fibrotic remodeling is occurring during this period. The expression of EGF family members, such as *Egf*, *Areg*, *Ereg*, and *Nrg1*, was upregulated in fibrotic tissues 2 weeks after irradiation (Fig. 3B). Among differentially expressed transcription factors, *Nfkb2*, *Relb*, Myc, *Stat1*, *Stat2*, *Stat4*, and *Stat5a* are associated with EGF signaling[32] (Fig. 3B).

Additionally, EGF signaling target genes were analyzed within the matrisome genes, and many of these, including fibrosis-related targets such as *Fn1*, *S100a4*, and *Serpine1*, were found to be upregulated during RIPF development, as shown in the heatmap (Fig. 3C). These results indicated that the expression of genes related to EGFR signaling and fibrotic process, as well as that of collagen genes, was upregulated during RIPF development. In addition, KEGG and GO enrichment analyses revealed increased enrichment of immune- and adhesion-related pathways, such as "Cytokine-cytokine receptor interaction" and "Cell adhesion molecules", under irradiation conditions (Fig. S5). These findings suggest enhanced immune signaling and cell-cell communication, which are consistent with active fibrotic remodeling[1,21]. Given the established role of EGF signaling in modulating both ECM dynamics and immune cell recruitment, these changes may reflect an EGF-driven crosstalk between fibrotic and immune responses in irradiated lung tissues.

Although genes such as Ccl2, Mmp9, and Fibronectin are typically upregulated during fibrosis, their expression appeared reduced in the RNA-seq data, likely due to extensive cell depletion in the fibrotic core at day 14 (Fig. 3C and Fig. S6A).

Immunohistochemical (IHC) analysis revealed that in irradiated fibrotic lung tissues, the basal levels of EGFR and ERBB3 increased more significantly than those of ERBB2 and ERBB4 when compared with that in nonirradiated lung tissues (Fig. S6B). Costaining with alveolar type 1 and type 2 markers showed a significant increase in EGFR and ERBB3 in T1a-positive type I alveolar epithelial (AT1) cells and pro-SPC-positive type II alveolar epithelial (AT2) cells (Fig. 3D). Moreover, the levels of phosphorylated EGFR and ERBG3 markedly increased in alveolar epithelial cells in irradiated fibrotic lung tissues (Fig. 3E). Although the levels of phosphorylated ERBB2 and ERBB4 increased in irradiated fibrotic lung tissues compared with that in nonirradiated tissues (Fig. 3E), the EGFR inhibitors sapitinib, afatinib, and dacomitinib, which share an N-phenylquinazolin-4-amine core structure, effectively inhibited the phosphorylation of EGFR and ERBB3 but not that of ERBB4, in irradiated fibrotic lung tissues, consistent with their inhibitory effects on RIPF (Fig. 3E and Fig. S6C). These results suggested that EGFR inhibitors with an N-phenylquinazolin-4-amine core structure may effectively inhibit RIPF by regulating the EGFR/ERBB3 axis in alveolar epithelial cells.

Based on our observations, we propose that the EGFR/ERBB3 axis plays a specific and crucial role in PF progression, particularly in epithelial cells. Furthermore, we suggest that N-phenylquinazolin-4-amine core structure-based EGFR inhibitors selectively regulate the EGFR/ERBB3 axis, thereby efficiently inhibiting the fibrotic process.

Monocyte-derived alveolar macrophages that secrete EGFR ligands accumulate during lung fibrosis

To examine the pattern of gene changes within the lung tissue during RIPF, we performed Kyoto Encyclopedia of Genes and Genomes (KEGG) pathway, and Gene Ontology (GO), and gene set enrichment analysis (GSEA) of the RNA-seq data presented in Fig. 4 and Fig. S6. Furthermore, we observed strong gene enrichment in myeloid cells and lymphocytes in lung tissues at 8, 11, and 14 d after irradiation compared with that in nonirradiated lung tissues. The expression of myeloid cell marker genes was upregulated 3.8-fold in irradiated lung tissues compared with that in nonirradiated lung tissue 14 d after irradiation (Fig. 4A). Moreover, the expression of lymphocyte cell marker genes was upregulated more than 2-fold in irradiated lung tissues (Fig. 4A). The gene expression of vascular endothelial cell, pericyte, and myofibroblast markers was downregulated at 14 d post-irradiation compared with that in the control (Fig. 4B), while the matrix fibroblast (MatrixFB) and distal epithelial cells (DISTALEP1) gene signatures were also downregulated at 14 d postirradiation during PF development (Fig. 4A). According to these results, we hypothesized that myeloid cells and lymphocytes contribute significantly to the development of fibrosis, in accordance with the loss of gene signatures corresponding to resident cells, such as vascular endothelial and epithelial cells. This apparent downregulation of resident cell markers may be attributed to cell depletion

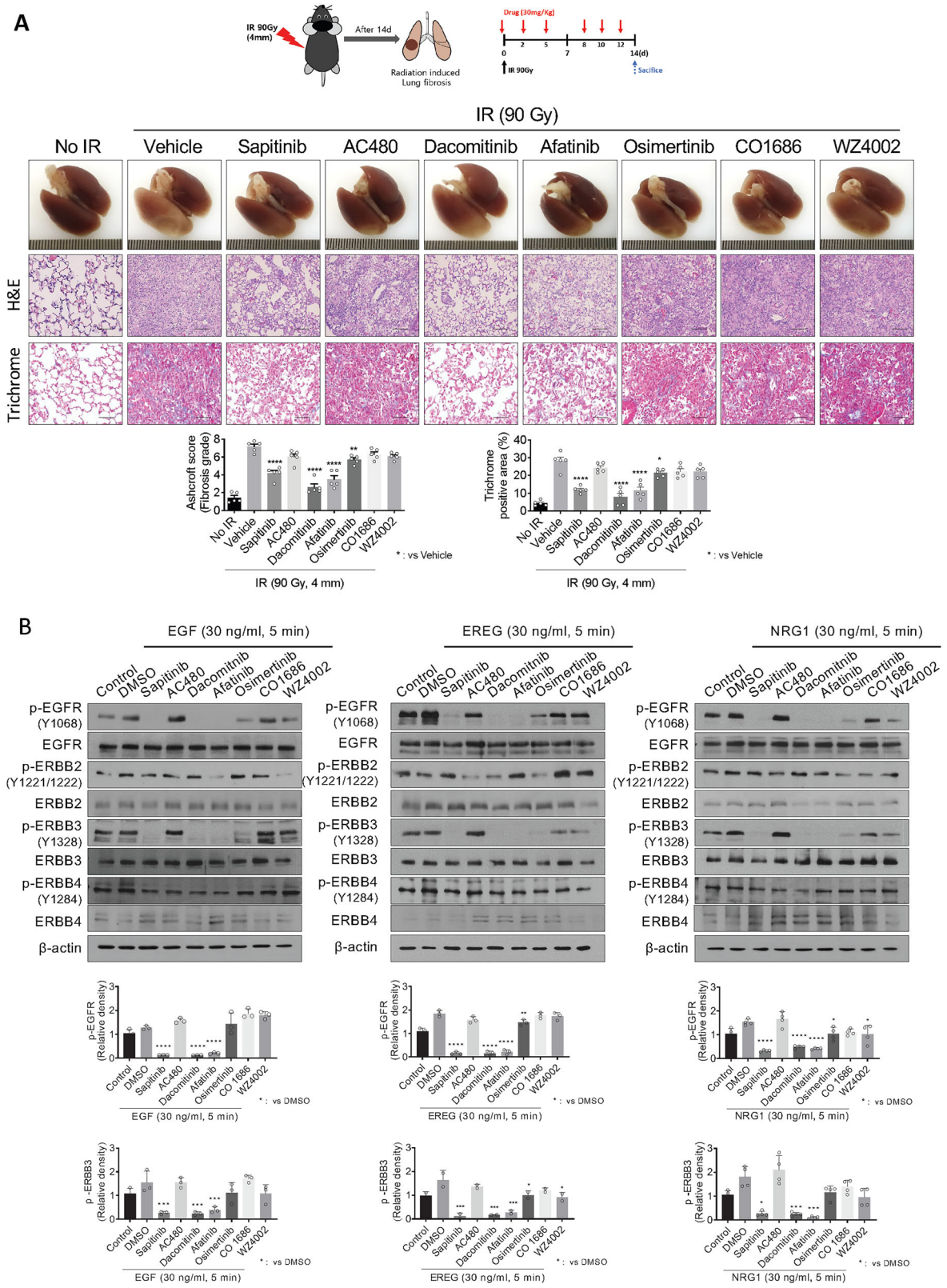

in the irradiated fibrotic core, rather than transcriptional repression. Notably, this shift coincided with a marked accumulation of myeloid and lymphoid populations, suggesting dynamic remodeling of cellular composition during fibrosis progression.

Next, we evaluated the expression of EGF family ligands in alveolar macrophages, whose potential involvement in fibrosis development was identified in the previous experiment, to investigate the link of EGFR signaling with potentially involved cell types. Interestingly, IHC analysis showed more prominent expression of EGF, EREG and NRG1 in alveolar macrophages in the nonirradiated area than in the targeted irradiation area (Fig. 4C). However, the detection of AREG was limited in both irradiated and nonirradiated lung tissues, although data analysis indicated a significant

Fig. 2 | EGFR TKIs differentially reduce radiation-induced lung fibrosis and inhibit EGFR/ERBB3 activity in HPAEps. A Schemes for the irradiation site in the mouse lung and drug administration. C57BL/6 mice were irradiated in the left main bronchus with 90 Gy using a 4 mm diameter field, and EGFR TKIs (30 mg/kg) were administered every 2–3 d for a total of 2 weeks ($n = 5$ animals per group). Mice were intraperitoneally injected with EGFR TKI and vehicle 1 h before irradiation. Representative images of the lungs; hematoxylin&eosin and Masson trichrome staining of lung tissues from C57BL/6 mice 2 weeks after irradiation with or without EGFR TKIs; scale bar = 100 μm. The fibrosis grade score is shown as an Ashcroft score graph. Collagen deposits were quantified using more than five fields (magnification: 200×). **B** HPAEps were treated with EGFR TKIs (1 μM) 1 h before treatment with the human-derived cytokines EGF, epiregulin, and NRG1 at 30 ng/mL for 5 min. Immunoblotting of EGFR, ERBB2, ERBB3, ERBB4, p-EGFR, p-ERBB2, p-ERBB3, p-ERBB4, and β-actin in HPAEps. The mean intensity of p-EGFR and p-ERBB3 from three independent experiments is given. In the Ashcroft score graph (**A**) and immunoblotting intensity graph (**B**), error bars indicate SD. In other graphs, error bars indicate SEM. Statistical significance was determined by one-way ANOVA with multiple comparisons (*$P < 0.05$, **$P < 0.01$, ***$P < 0.001$, ****$P < 0.0001$; ns, not significant).

Table 1 | EGFR TKI structure and respective targets

	Drugs	Structure	TK target
Anilino quinazolines Reversible inhibitors	Sapitinib		EGFR ERBB2 ERBB3
	AC480		EGFR ERBB2 ERBB4
Anilino quinazolines Irreversible inhibitors	Dacomitinib	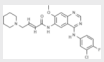	EGFR ERBB2 ERBB4
	Afatinib		EGFR ERBB2 ERBB4 Mutant EGFR
Anilino Pyrimidines Irreversible inhibitors	Osimertinib	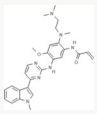	EGFR Mutant EGFR
	CO-1686	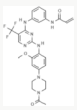	Mutant EGFR
	WZ4002	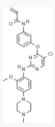	Mutant EGFR

The structures of EGFR TKIs and their respective targets. Compounds are divided into those with and without the N-phenylquinazolin-4-amine structure.

increase in AREG levels in irradiated tissues, similar to the results for the other EGF family ligands (Fig. 4C). These results suggested that EGF family ligands, including EGF, EREG, and NRG1, from accumulated macrophages may activate EGFR and ERBB3 in alveolar epithelial cells, thus contributing to RIPF progression.

Given the accumulation of alveolar macrophages and prior reports of functionally distinct macrophage activation states in fibrosis[19], we assessed whether macrophages expressing EGF ligands exhibited pro- or anti-inflammatory phenotypes. We examined the expression of iNOS (a marker of classically activated, pro-inflammatory macrophages) and arginase-1 (a marker of alternatively activated, anti-inflammatory macrophages) in irradiated lungs.

We found that iNOS-positive pro-inflammatory macrophages were present in irradiated and nonirradiated areas from the initial inflammatory phase 10 d after irradiation, prior to the fibrotic stage (Fig. 4D and Fig. S8A). However, we detected arginase 1^+ macrophages only in the irradiated fibrotic area in the fibrotic phase but not in the area surrounding the irradiated region. Conversely, $iNOS^+$ macrophages were readily detected in the nonirradiated region of irradiated lungs but not in the irradiated fibrotic tissue (Fig. 4E and Fig. S7A). Co-localization studies using CD80 and CD206 further supported the presence of functionally distinct macrophage subsets (Fig. S7B). These results indicate that pro-inflammatory- and anti-inflammatory macrophages accumulate in non-fibrotic and fibrotic regions, respectively, during the development of RIPF. The early accumulation of $iNOS^+$ pro-inflammatory macrophages suggest a role in initiating inflammation and potentially influencing the subsequent emergence of arginase-1^+ macrophages involved in chronic fibrosis progression. For macrophage lineage tracing, we used myelomonocytic cell-specific lysozyme M-Cre mice crossed to loxP-flanked tdTomato transgenic mice (Fig. 4F). Immunofluorescence (IF) revealed that macrophages co-expressing EGF, EREG, and NRG1 were predominantly found in $tdTomato^+$, $iNOS^+$ populations surrounding the irradiated region (Fig. 4F), while relatively fewer ligand-expressing macrophages were $Arg1^+$ in the fibrotic core (Fig. S7C). These results suggested that a large number of monocyte-derived alveolar macrophages with pro-inflammatory features expressing EGF ligands accumulate in the inflamed area surrounding the irradiated region, and that these cells may contribute to the increased EGFR and ERBB3 activity in alveolar epithelial cells during RIPF development.

Egfr/*Erbb3* knockdown inhibits the expression of cytokine storm-related genes and the expression EGF ligand genes in macrophages

Next, we determined whether *Egfr* or *Erbb3* knockdown directly affects fibrotic changes in primary human alveolar epithelial cells. A marked reduction in EGFR and ERBB3 protein expression following siRNA-mediated knockdown in HPAEps was confirmed by immunoblotting (Fig. S8A). EGFR or ERBB3 knockdown in HPAEps reduced the radiation-induced elongated fibrotic phenotype, marked by phalloidin and FSP1, as shown by IF (Fig. S8B), consistent with EMT/EndMT features in pulmonary fibrosis[25,33,34]. Interestingly, RNA-seq (deposited in the GEO repository, GSE306184) and GSEA showed that *Egfr* or *Erbb3* knockdown significantly decreased the TNF-α, IFN-γ, and IL-6 signaling related-gene expression in growth factor (EGF, EREG, and NRG1)-treated HPAEps. Additionally, in irradiated HPAEps, *Erbb3* but not *Egfr* knockdown, significantly down-regulated the expression of genes related to TNF-α, IFN-γ, IFN-α, and IL-6 signaling (Fig. 5A). At the individual gene level, RNA-seq confirmed the findings at the processing level, as the expression of inflammatory-related genes in HPAEps decreased under *Erbb3* or *Egfr* knockdown (Fig. 5B).

Radiation-induced lung acute injury can evoke the release of inflammatory cytokines via a process known as a radiation-induced cytokine storm[35]. In addition to prolonged cytokine storm, chronic inflammation may also lead to lung fibrosis[36]. Specifically, TNF-α, IFN-γ, and IL-6 are key cytokines whose levels are often elevated in cytokine storms[37]. In RIPF mouse models, IHC analysis of irradiated lung tissues showed that starting from the inflammatory stage 7 d after radiation exposure, the levels of TNF-α, IFN-γ, and IL-6 increased and continued to rise through the fibrotic stage at 14 d, persisting into late-stage fibrosis (Fig. 5C and Fig. S8C).

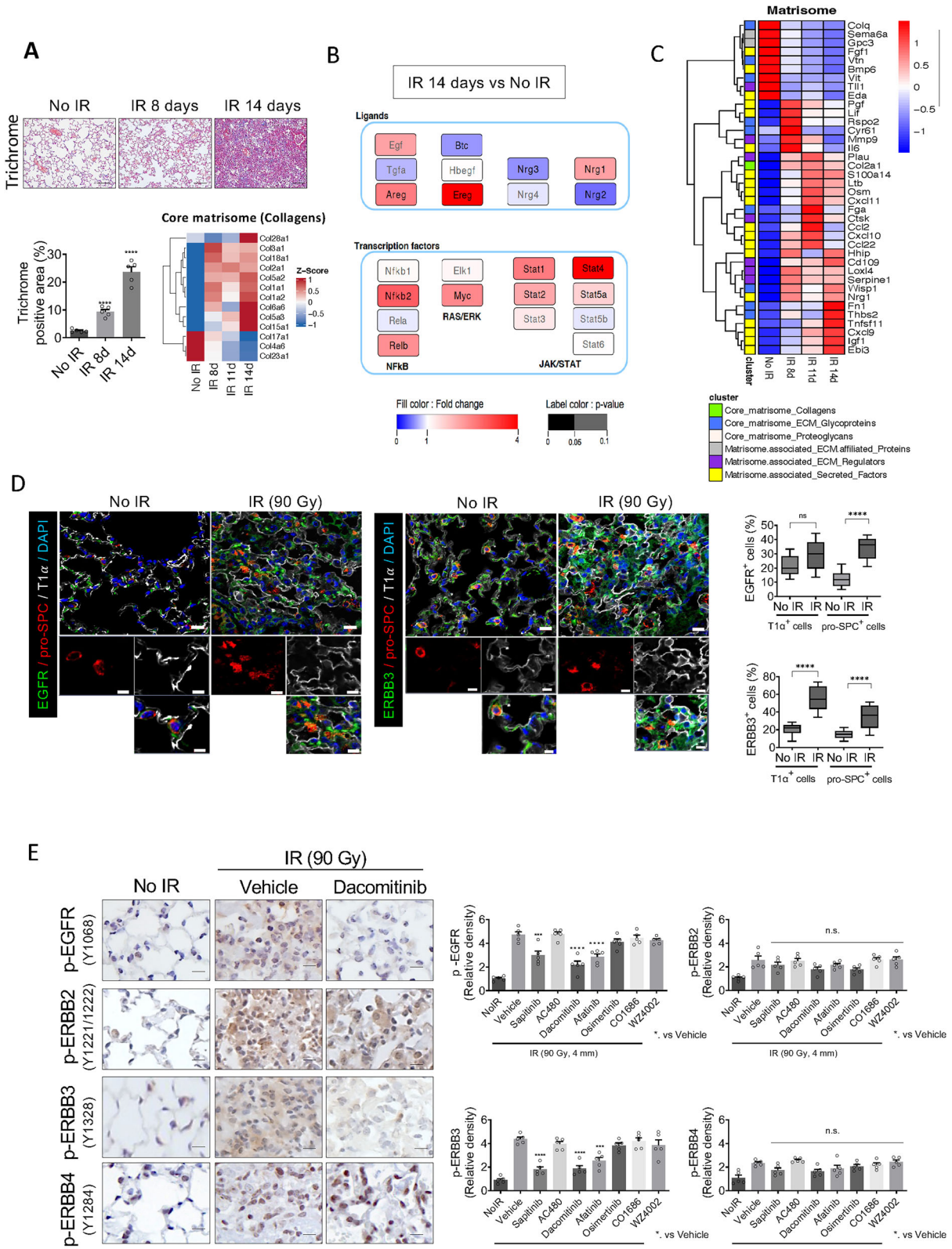

Additionally, the phosphorylation status of EGFR/ERBB3, which can regulate the expression of these cytokines, also increased during the fibrotic stages. The persistent activation of EGFRs in alveolar epithelial cells and the subsequent release of cytokines until the late fibrosis stage suggested their pathogenic role (Fig. 5C and Fig. S8D). Therefore, treatment with EGFR TKIs at the late stage could be beneficial.

Irradiated lung tissues from mice treated with sapitinib, afatinib, or dacomitinib were characterized by reduced levels of TNF-α, IFN-γ and IL-6 compared with those in irradiated tissues from vehicle-treated mice (Fig. 5D and Fig. S9E). Thus, EGFR inhibitors with an N-phenylquiazolin-4-amine core structure that impeded RIPF also decreased inflammatory cytokine levels. Additionally, we observed that treating THP-1 monocytes with

Fig. 3 | The EGFR/ERBB3 axis is activated in aveolar epithelial cells during PF development. A C57BL/6 mice were irradiated in the left main bronchus with 90 Gy using a 4 mm diameter field. Lung samples were obtained before (0 month) and 8 and 14 d after irradiation and used for RNA-seq analysis. Representative images of hematoxylin&eosin staining of lung tissues from C57BL/6 mice 8, 11, and 14 d after irradiation; scale bar = 100 μm. Graphs quantifying collagen deposition per field (magnification, 200×). Heat map of RNA-seq analysis showing differentially expressed collagen genes in one of the three irradiated conditions. **B** EGFR/ERBB signaling genes regulated by irradiation in lungs. Differentially expressed genes 14 d after irradiation were visualized with EGFR inhibitors using Cytoscape. **C** Heatmap of RNA-seq analysis showing differentially expressed matrisome genes in one of the three irradiated conditions (8, 11, and 14 d). **D** Immunofluorescence staining of EGFR (green), ERBB3 (green), pro-SPC (red), and T1α (white) was performed on irradiated and control lung tissues; scale bar = 10 μm; scale bar of cropped images = 5 μm. The graphs show EGFR- and ERBB3-positive cells among T1α- and pro-SPC-positive cell populations. **E** Immunohistochemistry staining of p-EGFR, p-ERBB2, p-ERBR3, and p-ERBB4 in the lung tissues of control and C57BL/6 mice 2 weeks after irradiation ($n = 5$ animals per group); scale bar = 20 μm; scale bar of cropped images = 5 μm. The average of five fields of p-EGFR, p-ERBB2, p-ERBB3, and p-ErbB4 density was quantified (magnification; 200×). In all graphs, statistical significance was determined by one-way ANOVA with multiple comparisons (*$P < 0.05$, **$P < 0.01$, ***$P < 0.001$, ****$P < 0.0001$; ns, not significant).

TNF-α, IFN-γ, and IL-6 led to an increase in the expression of EGF, EREG, and NRG (Fig. 5E). It is hypothesized that the increase in these cytokines in primary human epithelial cells subsequently enhanced the expression of EGF family ligands in monocytic macrophages. This suggested a feedback response where the sustained activation of EGF signaling in epithelial cells is maintained by the continuous expression of EGF family ligands by macrophages during the development of pulmonary fibrosis.

To examine the pro-inflammatory macrophage–epithelial feedback loop, we stimulated THP-1 cells with IFN-γ and LPS to induce a classically activated (pro-inflammatory) phenotype, and applied the resulting conditioned media to human alveolar epithelial cells. This treatment led to increased expression of fibrotic markers, including FSP1 and phosphorylated EGFR and ERBB3, as well as enhanced phalloidin intensity, indicating cytoskeletal reorganization, compared to controls and unactivated THP-1 conditioned medium. These results suggest that cytokines secreted by activated IFN-γ/LPS–activated macrophages promote fibrotic transformation in epithelial cells via EGFR and ERBB3 phosphorylation (Fig. S9).

These results suggested that EGFR TKIs targeting EGFR and ERBB3 can effectively inhibit RIPF development by decreasing the radiation-induced levels of the cytokine storm-related genes TNF-α, IFN-γ, IFN-α, and IL-6. Notably, Fig. 3 and Fig. 4 represent distinct experimental contexts —tissue-level transcriptomic profiling versus in vitro knockdown in epithelial cells—accounting for differences in cellular composition and gene expression patterns.

EGFR inhibitor inhibits BIPF with macrophages expressing EGF ligands

To investigate whether the EGFR/ERBB3 axis plays a crucial regulatory role in RIPF and the general progression of PF, we initially examined EGF expression in an BIPF mouse model using intratracheal bleomycin instillation. In addition, to determine whether the degree of fibrosis correlates with the accumulation of macrophage-expressing EGF ligands, we compared the differences in fibrosis extent (4 weeks) after injecting bleomycin at two different concentrations (1.25 and 1.6 U/kg) (Fig. 6A). The gray scale in microcomputed tomography (micro-CT) images showed lung injury in the BIPF group compared with that in the untreated group. Collagen deposition in trichrome staining depended on bleomycin concentration compared with that in the untreated group (Fig. 6A).

Moreover, the number of accumulated macrophages overexpressing the EGF ligands EGF, EREG, and NRG1 but not AREG, was proportional to the degree of fibrosis, as measured using the Aschroft score during BIPF development (Fig. 6A). The EGFR and ERBB3 activity also increased along with the fibrosis score (Fig. 6A and Fig. S10A). These results suggested that EGF ligand-activated EGFR and ERBB3 signaling in alveolar macrophages and epithelial cells may regulate cytokine release, thus contributing to IPF development.

Given the observed involvement of the EGFR axis in BIPF, we next examined the efficacy of EGFR inhibitors on BIPF. At 14 d after bleomycin administration, we assessed the degree of pulmonary fibrosis using micro-CT analysis. Afterward, we orally administered EGFR TKIs for two weeks and conducted weekly micro-CT analyses to track the efficacy of the drug in each individual (Fig. 6B). Pulmonary fibrosis (PF) lesions, as indicated by the progressive gray scale, were most effectively reduced by oral administration of 20 mg/kg dacomitinib, an EGFR TKI, which inhibited BIPF more efficiently than 60 mg/kg nintedanib (Fig. 6B). Quantitative assessment of in vivo micro-CT is presented in Hounsfield units (Fig. 6B, bottom graph). This was evidenced by the reduced collagen deposition and fibrotic progression (Fig. 6C). In addition, the antifibrotic effects of dacomitinib and nintedanib were validated through three independent RIPF experiments ($n = 5$ per group), which consistently demonstrated greater efficacy of dacomitinib in reducing fibrosis severity (Fig. S10B).

Dacomitinib decreases EGFR/ERBB3 phosphorylation and cytokine expression in alveolar epithelial cells in BIPF

Treatment with dacomitinib reduced the number of phosphorylated EGFR- and ERBB3-positive cells to a greater extent than nintedanib in lung tissues of BIPF mouse model (Fig. 7A). In bleomycin-induced pulmonary fibrotic tissues, a significant increase in EGFR and ERBB3 expression was observed compared with that in normal lung tissues, particularly in T1a-positive AT1 and pro-SPC-positive AT2 cells (Fig. 7B). Additionally, similar to the trends observed with EGFR and ERBB3, we also noted a significant increase in the expression of TNF-α, IL-6, and IFN-γ, particularly in T1a-positive AT1 and pro-SPC-positive AT2 cells, with IL-6 showing a notably high increase in AT2 cells (Fig. 7C). This suggested that these cytokines play an important role in the regulation within alveolar epithelial cells during the process of bleomycin-induced lung fibrosis. Interestingly, compared with the vehicle control, dacomitinib evoked a greater decrease in TNF, IL-6, and IFN-γ levels than nintedanib (Fig. 7D and Fig. S10C). These results suggested that the EGFR inhibitor dacomitinib may suppress BIPF more efficiently than the existing FDA-approved drugs for IPF by regulating cytokine levels.

This suggested that these cytokines play an important role in the regulation within alveolar epithelial cells during the process of bleomycin-induced lung fibrosis.

As shown Fig. 7E, we propose the scheme for the crosstalk between pro-inflammatory macrophages and alveolar epithelial cells in pulmonary fibrosis progression. Under initial inflammatory stimuli, macrophages with pro-inflammatory phenotypes secrete EGFR ligands, leading to their accumulation in the damaged area. This causes prolonged activation of EGFR/ERBB3 on type I and type II alveolar epithelial cells, inducing fibrosis. Additionally, the increase in TNF-α, IFN-γ, and IL-6 from epithelial cells acts as a feedback signal to enhance the gene expression of EGFR ligands in macrophages. This feedback loop is proposed to result in chronic fibrosis.

EGFR TKI dacomitinb inhibits RIPF by enhancing tumor radioresponse in image-guided radiation therapy (IGRT)

To investigate the potential for simultaneous RIPF regulation and enhancement of radiation therapy efficacy in clinical settings, we performed IGRT in a spontaneous lung tumor model. A single-nodule NSCLC tumor was generated via intrathoracic application of a replication-deficient adenovirus expressing Cre (Ad-Cre) to initiate oncogenic K-RasG12D activation and deletion of both copies of a conditional p53 (p53 flox) allele using the Cre-loxP system (Fig. 8A). A total radiation dose of 45 Gy was delivered in three fractions to the left lung tumor using a 5-mm collimator to protect the opposite lung and spinal cord (Fig. 8B). We observed micro-CT manifestations of radiation-induced lung injury, such as ground-glass opacities and pulmonary consolidation, four weeks following focal irradiation of 45 Gy (Fig. 8C). These manifestations were significantly attenuated by

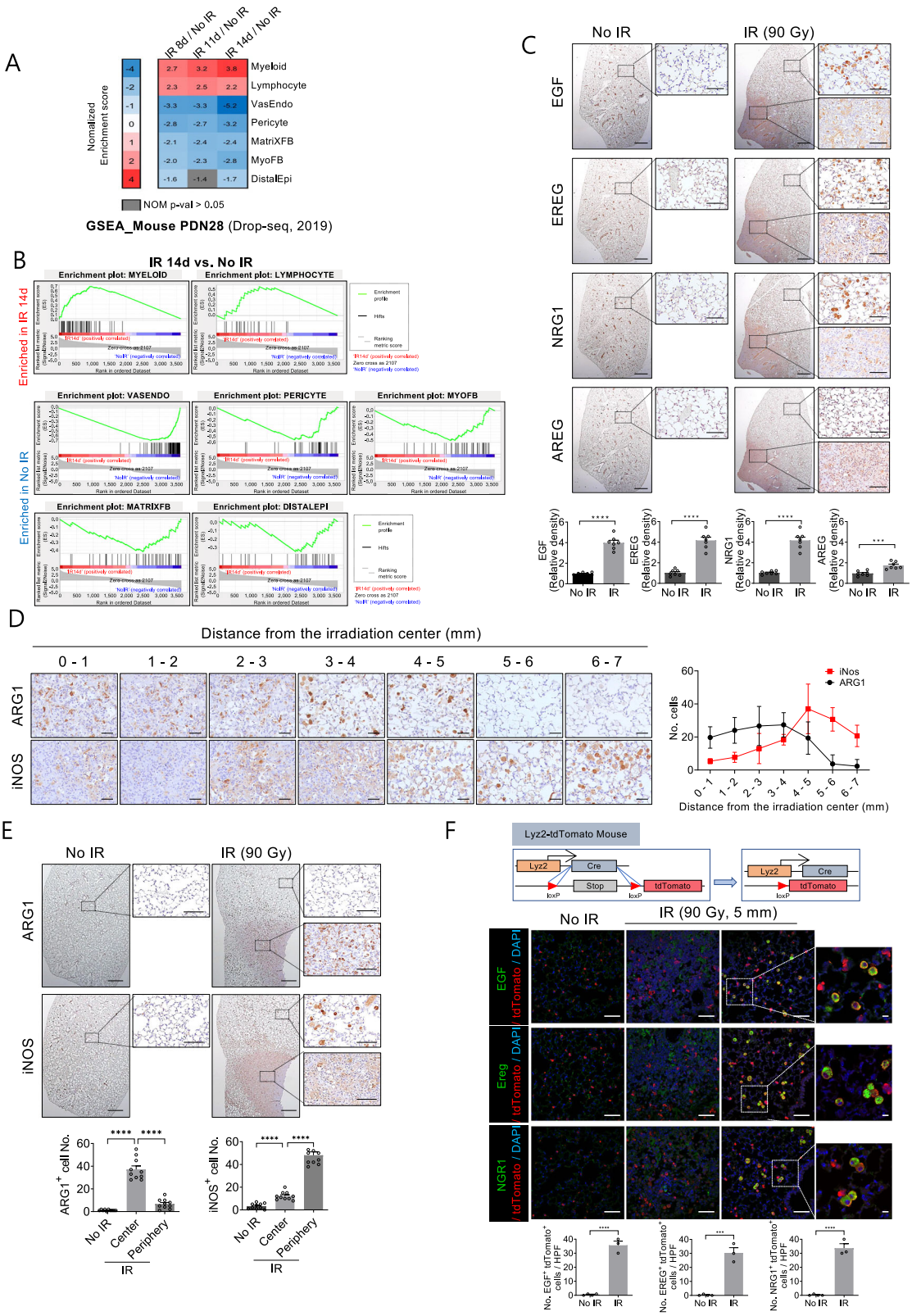

concurrent oral administration of dacomitinib, accompanied by a significant inhibition of tumor growth compared with that in nonirradiated lungs. Moreover, combined treatment with dacomitinib resulted in a greater preservation of normal lung volume after IGRT compared with that after treatment with vehicle. Therefore, our findings highlighted the potential of specific EGFR inhibitors in clinical use as promising therapeutics for PF.

Additionally, to enhance the translational relevance of our findings, we established human organotypic fibrosis models using 3D lung organoids composed of co-cultured human monocytes, fibroblasts, and alveolar epithelial cells. Upon bleomycin treatment, these organoids exhibited increased FSP1 and phalloidin expression along with structural distortion. Treatment with nintedanib reduced these fibrosis markers, while dacomitinib resulted

Fig. 4 | Monocyte-derived alveolar macrophages expressing EGF, Ereg, and NRG1 accumulate in irradiated lung tissues. GSEA of cell type-specific genes in irradiated lungs compared with nonirradiated control. **A** Heat map showing normalized enrichment scores with normalized *P* value < 0.05. **B** Enrichments plots 14 d after irradiation. **C** Immunohistochemistry staining of EGF, EREG, NRG1, and AREG in the lung tissues of control and C57BL/6 mice 2 weeks after irradiation ($n = 7$ animals per group); scale bar = 1 mm; scale bar of cropped images = 100 μm. The average of five fields of EGF, EREG, NRG1, and AREG density was quantified (magnification: 200×). **D** Immunohistochemistry staining of ARG1 and iNOS in lungs from the irradiated and nonirradiated portions ($n = 3$ animals per group); scale bar = 50 μm. **E** Immunohistochemical detection of ARG1 and iNOS in the lung tissues of control and C57BL/6 mice 2 weeks after irradiation; scale bar = 1 mm; scale bar of cropped images = 100 μm. Quantification of average more than five fields of ARG1- and iNOS-positive cell numbers (magnification: 200×). **F** Scheme of Lyz2-Cre;tdTomato mice. These mice were generated by crossing Lyz2-Cre and CAG-tdTomato mice. Immunofluorescence staining of EGF, EREG, NRG1, and tdTomato in lung tissues; scale bar = 100 μm; scale bar of cropped images = 20 μm. In (**C**) and (**F**), data are presented as mean SD, and comparisons were made using a two-tailed Student's t-test. In (**E**), statistical significance was determined by one-way ANOVA with multiple comparisons ($^{*}P < 0.05$, $^{**}P < 0.01$, $^{***}P < 0.001$, $^{****}P < 0.0001$; ns, not significant).

in a more pronounced reduction, supporting its stronger antifibrotic effect (Fig. S11). These results provide additional functional validation using a human-based fibrosis model.

Discussion

The mortality associated with IPF is steadily increasing worldwide[38]. Therefore, the urgent need for the development of targeted IPF therapies becomes evident. However, the current situation indicates that existing treatments, such as nintedanib and pirfenidone, cannot overcome their limitations[39]. The novelty of this study lay in the discovery of specific inhibitors that appear to selectively inhibit particular ERBB family receptor tyrosine kinases (RTKs) at the protein level on pulmonary epithelial cells. These inhibitors have demonstrated efficacy in various models of pulmonary fibrosis and have established a connection between ERBB family signaling and specific immune-mediated responses.

EGFR TKI compounds with the N-phenylquinazolin-4-amine structure, currently used in clinical practice, markedly alleviated RIPF by inhibiting the EGFR and ERBB3 activity in lung epithelial cells. Macrophage EGF ligand levels and epithelial cell EGFR and ERBB3 activity were proportional in the BIPF model. Furthermore, the EGFR and ERBB3 activity regulated the IL-6, IFN-γ, and TNF-α levels during PF development in animal models of RIPF and BIPF. Additionally, the phosphorylated EGFR and ERBB3 levels were higher in tissues from patients with RIPF and BIPF than in those from control participants. Here, we first found that EGFR inhibitors with an N-phenylquinazolin-4-amine structure exerted inhibitory effects on RIPF and reduced EGFR and ERBB3 phosphorylation in alveolar epithelial cells. Third-generation EGFR inhibitors that target mutant EGFR, such as osimertinib, have different core structures; interestingly, several third-generation EGFR inhibitors did not inhibit EGFR and ERBB3 phosphorylation in alveolar epithelial cells and RIPF in this study. Notably, although AC480 retains the N-phenylquinazoline core structure, it did not exhibit significant antifibrotic activity in our model. This discrepancy may be attributed to differences in its side chain, which could influence its antifibrotic activity. To address this, we are currently planning structure–activity relationship (SAR) studies to clarify its impact on EGFR/ERBB3 signaling and antifibrotic efficacy.

The N-phenylquinazolin-4-amine core structure is predominantly seen in first- and second-generation EGFR TKIs designed to target NSCLC tumor cells[40]. These drugs primarily aim to inhibit EGFR, ERBB2, and ERBB4. However, ERBB3, characterized by its pseudokinase domain and relatively low kinase activity, has not been extensively studied as a target for EGFR TKI drug development[41]. We showed that EGFR TKIs with the core structure specifically inhibited EGFR and ERBB3 phosphorylation, thus regulating STAT5 signaling in alveolar epithelial cells. This study suggested that coregulation of EGFR and ERBB3 in alveolar epithelial cells is crucial for PF progression. Moreover, understanding the precise mechanism governing this coregulation is essential for developing EGFR TKIs as an effective therapeutic agents to control PF. Our future study will focus on understanding why this specific type of inhibitor might exhibit a different inhibitory effect compared with other ERBB family inhibitors.

Furthermore, this study emphasized the significance of understanding the crosstalk between immune and epithelial cells in PF regulation. Upon irradiation, an inflammatory response occurs in lung tissue prior to the fibrotic response, and each of these responses is governed by a specific type of macrophages. Our study showed that the macrophages expressing EGF ligands during the inflammatory response were iNOS-positive pro-inflammatory macrophages, whereas these ligands were not expressed by arginase-1-positive macrophages in the fibrotic region. From these observations, we hypothesized that pro-inflammatory macrophages begin secreting EGF family ligands during the early inflammatory stages of lung injury, leading to hyperphosphorylation of EGFR/ERBB3 in damaged alveolar epithelial cells and inducing tissue fibrosis, including the fibrotic change of epithelial cells. In late fibrotic tissues, the profibrotic activity of arginase-1^{+} macrophages is considered more significant than the EGF growth factor secreted by early-stage macrophages in the fibrotic environment. We propose that pro-inflammatory macrophages also play a crucial promoting role throughout the fibrotic process, starting from the early stage of lung inflammation.

Based on our RNA-seq data, we observed that *Egfr* and *Erbb3* knockdown significantly decreased the expression of genes associated with IL-6, IFN-γ, and TNF-α signaling upon radiation treatment, as well as that of the growth factors EGF, EREG, and NRG. Moreover, the cytokines IL-6, IFN-γ, and TNF-α were detected in the fibrotic areas of RIPF and BIPF tissues. These cytokines play a critical role in cytokine storms, highlighting their importance in the inflammatory response[42]. Cytokine storms are well recognized as acute responses after lung injury. However, prolonged expression of these cytokines may be important for the pathogenesis of fibrosis[43,44]. The precise mechanism, by which EGFR and ERBB3 regulate cytokine levels during PF development, remains unclear; however, we are currently investigating this topic.

The RIPF model offers the advantage of a consistent degree and timing of PF in the irradiated area, dependent on the dose and volume of radiation[45]. This allows for the observation of various phenomena in the surrounding tissues throughout the fibrotic process. The efficacy of EGFR TKIs in the RIPF model was consistent with the results observed in the BIPF animal model.

Although clinical reports have documented interstitial lung injury as a side effect of several EGFR TKIs, the consideration of several factors, including concurrent chemotherapy, tumor response, and patient immune status is essential. Therefore, our current research focuses on the development of a prodrug formulation for EGFR TKIs. This formulation is designed to facilitate effective drug delivery to fibrotic tissues at lower concentrations, thereby maximizing the therapeutic efficacy of EGFR TKIs in controlling fibrosis.

From the analysis of a recently published scRNA dataset, we propose that aberrant basaloid cell types exhibiting elevated expression of EGF-related genes play a significant role in IPF. Alveolar epithelial cells are recognized as key contributors to PF pathogenesis through processes, such as EMT and senescence[46]. Our findings also demonstrated that EGFR and ERBB3 regulate the radiation-induced EMT phenotype of alveolar epithelial cells.

While EGFR signaling has been previously implicated in pulmonary fibrosis, our study provides novel mechanistic insights by focusing on N-phenylquinazolin-4-amine-based EGFR TKIs that selectively target ERBB3 and preferentially inhibit STAT5 signaling. We also propose a previously uncharacterized pro-inflammatory macrophage–epithelial feedback loop that may contributes to sustained EGFR/ERBB3 activation and chronic cytokine production during fibrotic progression. These findings suggest that persistent EGFR/ERBB3 signaling links inflammatory cytokine responses to fibrosis. Importantly, our results highlight the potential of repurposing FDA-approved EGFR inhibitors as antifibrotic agents. A deeper understanding of

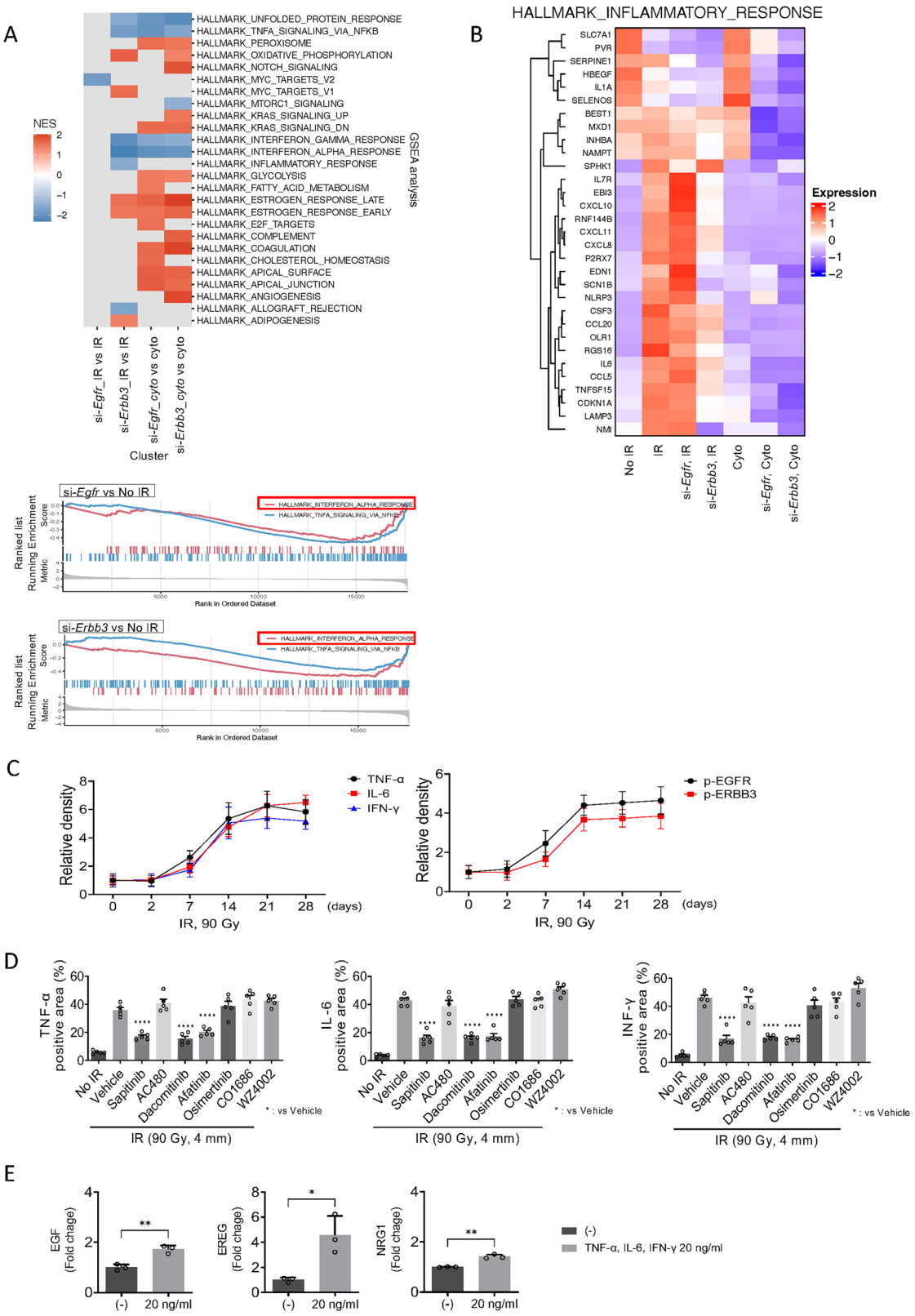

EGFR/ERBB3 signaling in epithelial and immune cells may accelerate the development of targeted therapies for pulmonary fibrosis.

Methods

For more details on the "Methods", refer to the online supplementary materials and methods.

RIPF model

Radiation was administered using the X-RAD 320 (Precision X-ray, North Branford, CT, USA). The left main bronchi of 7- to 8-week-old mice were irradiated with 90 Gy using a 4 mm diameter field. C57BL/6 mice were treated intraperitoneally with 30 mg/kg of EGFR TKIs 1 h before the irradiation and continually treated every 2–3 d for a total of

Fig. 5 | *Egfr/Erbb3* knockdown inhibits the expression of cytokine storms-related genes in HPAEps and the expression of EGF, EREG and NRG1 genes in macrophages is regulated by these cytokines. HPAEps were transfected with *Egfr*- or *Erbb3*-siRNA and irradiated with 10 Gy or treated with cytokines (EGF, EREG, and NRG1) for 3 d. Cells ($n = 2$/group) were harvested and used for RNA-seq analysis. **A** GSEA of Hallmark pathway genes in epithelial cells. Heat map showing normalized enrichment scores with normalized P value < 0.05, and enrichments plots of *Egfr*- or *Erbb3*-knockdown epithelial cells compared with control. **B** Heat map of RNA-seq analysis showing differentially expressed Hallmark pathway genes in one of the four comparisons (*Egfr*si + IR/IR, *Erbb3*si + IR/IR, *Egfr*si+cyto/cyto, and *Erbb3*si+cyto/cyto). **C** Immunohistochemistry staining of TNF-α, IL-6, INF-γ, p-EGFR and p-ERBB3 in lung tissues of control and C57BL/6 mice after irradiation. The graphs indicate that C57BL/6 mice were irradiated after 2, 7, 14, 21, and 28 d; scale bar = 20 μm; The average of five fields of TNF-a, IL-6, IFN-r, p-EGFR, and p-ERBB3 density were quantified (magnification; 200×). **D** Immunohistochemistry staining of TNF-α, IL-6, and INF-γ in the lung tissues of control and C57BL/6 mice 2 weeks after irradiation ($n = 5$ animals per group); scale bar = 25 μm. The graphs indicate that C57BL/6 mice were intraperitoneally treated with EGFR TKIs starting 1 h before irradiation; immunohistochemical detection of TNF-α, IL-6, and INF-γ in the lung tissues of control and C57BL/6 mice 2 weeks after irradiation. The average of five fields of TNF-α, IL-6, and INF-γ density was quantified (magnification: 200×). **E** RT-qPCR analysis of EGF, EREG, and NRG1 in THP-1 cells treated or not with 20 ng/mL TNF-α, IL-6, and IFN-γ, respectively. In (**D**), statistical significance was determined by one-way ANOVA with multiple comparisons (*$P < 0.05$, **$P < 0.01$, ***$P < 0.001$, ****$P < 0.0001$; ns, not significant). In (**E**), data are presented as mean SD, and comparisons were made using a two-tailed Student's t-test.

six times. The EGFR TKIs used were sapitinib (#S2192; Selleckchem, city, [state], country), AC480 (#S1056; Selleckchem), dacomitinib (#S2727; Selleckchem), afatinib (#S1011; Selleckchem), osimertinib (#S7297; Selleckchem), CO1686 (#S7284; Selleckchem) and WZ4002 (#S1173; Selleckchem) dissolved in 5% (v/v) dimethylsulfoxide + 30% (w/v) polyethylene glycol 300 + 1% (v/v) Tween-80 in ddH_2O immediately before injection.

BIPF model

Six-week-old male mice (C57BL/6) were purchased from the Orient Bio Inc. (Orient Bio Inc., Seongnam, Korea). Bleomycin (1.6 U/kg; #B5507; Sigma, Burington, MA, USA) in 60 μL PBS was injected intratracheally into mice. Mice were injected intraperitoneally with 20 mg/kg of EGFR TKIs and 60 mg/kg nintedanib (#S1010; Selleckchem) 14 d after bleomycin administration. Drugs were orally administered daily for 2 weeks.

Mice and ethical approval

All animal experiments are reported in accordance with the ARRIVE guidelines. Mice experiments were approved by the Institutional Animal Care and Use Committee of the Korea Institute of Radiological & Medical Sciences (Kirams 2020-0014, 2021-0093, 2022-0099). We have complied with all relevant ethical regulations for animal use. Specific pathogen-free C57BL/6 Lyz2-Cre, CAG-tdTomato, LSL-$Kras^{G12D}$, and $Trp53^{flox/flox}$ mice were purchased from the Jackson Laboratory (Bar Harbor, ME, USA). Lyz2-Cre;tdTomato mice were generated by crossing Lyz2-Cre mice with CAG-tdTomato mice. $Kras^{G12D}$;$Trp53^{flox/flox}$ mice were generated by crossing $Trp53^{flox/flox}$ mice with LSL-$Kras^{G12D}$ mice. All animal experimental data provided are representative of three independent experiments. All experiments were conducted using 6–8-week-old mice of either sex, and mice were maintained on a 12 h light-dark cycle in a standard environment (20 ± 1 °C room temperature, 50 ± 10% relative humidity) provided a standard diet and water ad libitum. All mice were anesthetized using a combination of anesthetics before being euthanized.

Small animal irradiation planning and IGRT

The left lung tumor of mice was subjected to radiation (15 Gy, once a day for 3 d) using an image-guided precision irradiator (XRAD-SmART, Precision X-ray, North Branford, CT, USA). This X-ray irradiation system was equipped with cone beam computed tomography (CBCT) capability and a movable stage, allowing precise irradiation with a small field using a precision collimator. To protect the contralateral lung and spinal cord, radiation delivery was planned to the target using an opposing tangential field and a 5-mm collimator[47].

Immunohistochemistry and immunofluorescence staining

Tissues were fixed in 10% (v/v) neutral buffered formalin, embedded in paraffin, and sectioned. Tissue slides were deparaffinized and stained with haematoxylin and eosin and Masson's trichrome stain (Polyscience; #25088-100). IHC staining of deparaffinized sections was performed in antigen retrieval citrate buffer (Sigma; #C9999) at 95 °C for 30 min. After washing, the tissues were incubated with 0.3% (v/v) hydrogen peroxide in methanol for 15 min. Tissue slides were permeabilized for 15 min with PBS containing 0.1% Triton X-100 (PBST) and blocked in PBST containing normal horse serum at room temperature for 30 min. IF staining followed the same procedure as IHC, but the 0.3% H_2O_2 step was omitted. Next, the primary antibodies were diluted in blocking buffer and reacted overnight at 4 °C. For IHC staining, brown color was developed using ABC kit (Vector; #PK-6100) and DAP kit (Vector; #PK-4100) after secondary antibody reaction, and nuclei were stained with haematoxylin. IF staining was detected with fluorescent secondary antibodies, and nuclei were stained with DAPI (Sigma; #D9542). For quantification, a minimum of five images were acquired per section, and positively stained areas were measured with ImageJ software (NIH, Bethesda, MD; http://imagej.net/).

Antibodies for immunoblotting, immunofluorescence, and immunohistochemistry staining

Immunoblotting, IHC, and IF staining were performed using primary antibodies against p-EGFR (IHC 1:100; immunoblotting 1:1000; Cell Signalling; #2234S), EGFR(IHC 1:100; immunoblotting 1:1000; Santa Cruz Biotechnology; #sc102), p-ERBB2 (IHC 1:200; immunoblotting 1:1000; Novusbio; #NB100-89474), ERBB2 (IHC 1:100; immunoblotting 1:1000; Cell Signalling; #2165), p-ERBB3 (IHC 1:200; immunoblotting 1:2000; Abcam; #ab131444), ERBB3 (IHC 1:100; Invitrogen; #MA5-13008), p-ERBB4 (IHC 1:200; immunoblotting 1:1000; Abcam; #ab61059), ERBB4 (IHC 1:200; immunoblotting 1:1000; Abcam; #ab19391), pro-SPC (IF 1:200; Merck; #AB3786), T1a (IF 1:200; R&D System; AF3244), arginase-1 (IHC/IF 1:2000; Novusbio; #NBP1-32731), iNOS (IHC/IF 1:100; Santa Cruz Biotechnology; #sc7271), TNF-α (IHC/IF 1:100; R&D System; #AF-410NA), IL-6 (IHC/IF 1:200; Abcam; #ab208113), IFN-γ (IHC/IF 1:200; Abcam; #ab216642), EGF (IHC/IF 1:100; Santa Cruz Biotechnology; #sc166779), EREG (IHC/IF 1:100; Santa Cruz Biotechnology; #sc376284), NRG1 (IHC/IF 1:200; Invitrogen; #MA5-12896), AREG (IHC/IF 1:200; R&D System; #AF989), FSP (IF 1:200; Novus; NBP2-54580AF488), Fibronectin (IHC1:100; Abcam; #ab2413), MMP9 (IHC; 1:100 santa Cruz Biothechnology #sc6841), tdTomato (IF1:10,000; LSbio; #LS-C340696), and β-actin (immunoblotting 1:1000; Abcam; #ab8226). Actin stress fibers in cells were stained with Alexa Fluor 546-conjugated phalloidin (1:200; Invitrogen; #A22283), which specifically binds F-actin.

Cell culture and treatment

HPAEps were purchased from Cell Biologics (#H6053) and cultured in epithelial cell growth medium (cell biologics; #H6621) under 5% CO_2, 37 °C. HPAEps were used in passages 8–12. For irradiation, cells were exposed to gamma rays derived from a 137Cs source (Atomic Energy of Canada, Mississauga, ON, Canada) at a dose rate of 3.81 Gy/min. Lipofectamine 2000 (Invitrogen; #11668019) was used as a transfection reagent,

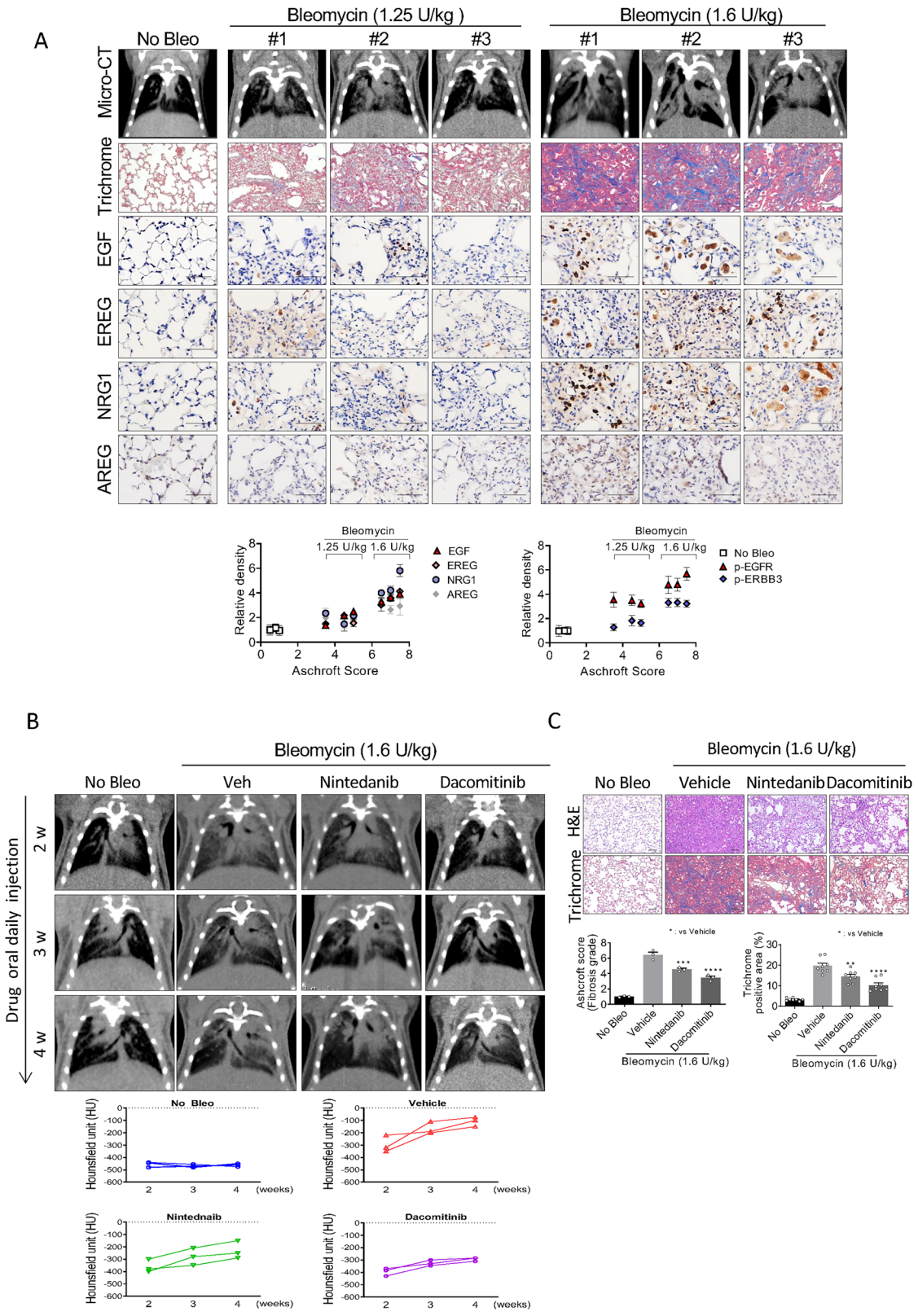

and *EGFR* siRNA (Santa Cruz Biotechnology; #sc-29301), *ERBB2* siRNA (Santa Cruz Biotechnology; #sc-29405) *ERBB3* siRNA (Santa Cruz Biotechnology; #sc-35327), *ERBB4* siRNA (Santa Cruz Biotechnology; #sc-35329), *STAT5* siRNA (Santa Cruz Biotechnology; #sc-29495), and control siRNA (Santa Cruz Biotechnology; #sc-37007) were transfected.

For cytokine treatment, HPAEps were starved with OPTI-MEM (Gibco; #11058021) for 2 h. Next, 1 h after EGFR TKI (1 μM) treatment, the cytokines EGF (30 ng/mL; Sigma-Aldrich; #E9644), EREG (30 ng/mL; R&D System; #1195-EP/CF), and NRG1 (30 ng/mL; Origene; #TP721215) were administered, and prep was performed after 5 min.

Fig. 6 | The degree of fibrosis correlates with the accumulation of macrophage-expressing EGF ligands and dacomitinib inhibits BIPF more efficiently than nintendanib. A Bleomycin (1.25 and 1.6 U/kg) in 50 μL PBS was injected intratracheally into mice. Micro-CT images show inflammatory- and fibrosis-phase mouse lungs after bleomycin administration. Masson's trichrome staining and immunohistochemical detection of EGF, EREG, NRG1, and AREG in inflammatory- and fibrotic-phase mouse lungs after bleomycin administration; scale bar of trichrome image = 100 μm; scale bar of immunohistochemistry image = 2.5 μm. The density of EGF, EREG, NRG1, AREG, p-EGFR, p-ERBB3, and p-ERBB4 was quantified according to the Ashcroft score (magnification: 200×). **B** Mice were injected orally with EGFR TKIs (20 mg/kg) and nintedanib (60 mg/kg) 14 d after bleomycin administration. Drugs were administered orally daily for 2 weeks. Micro-CT images depict the lungs of mice after bleomycin injection after 2, 3, and 4 weeks in the fibrosis phase. The graphs show Hounsfield units (HU) for each group. **C** Hematoxylin&eosin and Masson's trichrome staining of lung tissues from C57BL/6 mice 4 weeks after bleomycin injection treated with or without dacomitinib and nintedanib; scale bar = 100 μm. Fibrosis grade scoring and collagen deposition quantification per field (magnification: 200×) are shown. In the Ashcroft score graph (**C**), error bars indicate SD. Statistical significance was determined by one-way ANOVA with multiple comparisons (*$P < 0.05$, **$P < 0.01$, ***$P < 0.001$, ****$P < 0.0001$; ns, not significant).

THP-1 were obtained from Korean Cell Line Bank (#40202). THP-1 cells were treated with TNF-α, IL-6 and IFN-γ (20 ng/ml, respectively) 4 h. Four hours later, the mRNA levels of EGF, EREG, and NRG1 were assessed using RT-qPCR (Bio-Rad CFX Maestro).

THP-1 cells were treated with PMA (61 ng/ml) for 6 h to differentiate into the M0 transition stage and treated with IFN-r (5 ng/ml) and LPS (10 ng/ml) for 18 h to differentiate into the pro-inflammatory stage. After 24 h of culture, the culture medium obtained from THP-1 cells was treated to epithelial cells and then cultured for an additional 24 h[48].

96-well plates were pre-coated with a 40% solution of growth factor-reduced Matrigel (Corning) diluted in maintenance medium and incubated at 37 °C for 45 min. Following gelation, a single-cell suspension composed of primary human pulmonary alveolar epithelial cells (HPAEps, Cell Biologics; #H6621), human pulmonary microvascular endothelial cells (HPMECs, Promocell; C-12281), and human pulmonary fibroblasts (HPFs, Promocell; C-12360) was prepared in HAPEps medium supplemented with 5% Matrigel. A total of 1×10^5 HPAEps, 0.7×10^5 HPMECs, and 0.2×10^5 HPFs (in a ratio of 10:7:2) were seeded onto the Matrigel layer. Three days prior to bleomycin treatment, THP-1 monocytic cells were added to the culture to simulate immune cell involvement. One hour before bleomycin (10 mUnit/ml) treatment, cells were pre-treated with Dacomitinib and Nintedanib at a final concentration of 1 μM. Immunofluorescence (IF) staining was performed seven days after bleomycin administration[49].

RT-qPCR analysis

Total RNA was extracted with Qiazol Lysis Reagent (#79306, Qiagen) and subsequently converted into cDNA using the amfiRivert cDNA Synthesis Platinum Master Kit (R5600, GenDEPOT). PCR was conducted in triplicate on the CFX96 TM Real-Time system (Bio-Rad, Hercules, CA, USA), using qPCR SYBR Green master mix (Invitrogen). Glyceraldehyde 3-phosphate dehydrogenase (GAPDH) was used as a housekeeping gene. The sequences for forward and reverse primers were the following: GAPDH F: 5′-CAAGAAGGTGGTGAAGCAGG-3′ and R: 5′-AGGTGGAAGAGTGGGAGTTG-3′; EGF F: 5'-ACAGAATCTCAACACATGCTACT-3' and R: 5'-CATCCTCTCCCTCTGAAAYACAC-3', EREG F: 5'-TCATGTATCCCAGGAGAGTCC-3' and R: 5'- CAGAGCTACACTTTGTTATTGACAC-3' and NRG1 F: 5'-GTAAAATGTGCGGAGAAGGAGA-3' and R: 5'-CAGCGATCACCAGTAAACTCA-3'.

RNA-seq analysis

Total RNA was isolated and RNA quality was assessed using an Agilent 2100 Bioanalyzer (Agilent Technologies) for mouse lung tissue. RNA-seq libraries were constructed using the SMARTer Standard RNA-Seq Kit (Clontech) according to the manufacturer's instructions, and they were sequenced as 100 bp paired-end runs using HiSeq 2500 (Illumina, Inc., USA). RNA-seq reads were mapped to UCSC mm10 using TopHat software[50]. Genes with a maximal $\log_2$-transformed read count <3 across samples were excluded from the analysis. We used the criterion $|\log_2 FC| > 1$ to identify differentially expressed genes by comparing the irradiated and non-irradiated groups. Among the differentially expressed genes, ERBB signalling-related genes were displayed in Cytoscape 3.7.1[51] and R using the "pheatmap" package (v1.0.12). Matrisome gene lists were used to analyze microenvironmental changes in irradiated lung tissues. The matrisome comprises core matrisome-related proteins, including ECM glycoproteins, collagens, and proteoglycans, as well as ECM-associated proteins, including ECM-affiliated proteins, ECM regulators, and secreted factors[52]. Cell type-specific signature genes in mouse lung at age P27 were downloaded from LGEA web portal[53,54] and used for GSEA (4.0.2)[55]. KEGG pathways and GO term analyses were conducted using clusterProfiler (v4.12.6)[56].

For epithelial cells, total RNA was isolated, and RNA quality was assessed using an Agilent 2100 Bioanalyzer (Agilent Technologies). RNA-seq libraries were constructed using the SMARTer Standard RNA-Seq Kit (Clontech) according to the manufacturer's instructions, and they were sequenced as 100 bp paired-end runs using HiSeq 2500 (Illumina, Inc., USA). RNA-seq reads were mapped to UCSC hg19 using TopHat software[50].

The differentially expressed genes were identified in R (v1.0.12) using the "edgeR" package (v.3.32.1)[57] with the criterion $|\log_2 FC| > 1$. GSEA (clusterProfiler v.3.16.1)[56] was performed using Hallmark pathway genes from the "msigdbr" package (v.7.4.1)[58]. msigdbr: MSigDB Gene Sets for Multiple Organisms in a Tidy Data Format. R package version 7.4.1. https://CRAN.R-project.org/package=msigdbr), and the significant pathways were displayed using "Enrichplot" (v.1.8.1)[56] (enrichplot: Visualization of Functional Enrichment Result. R package version 1.12.2, https://yulab-smu.top/biomedical-knowledge-mining-book/) and "ComplexHeatmap" (v.1.20.0)[59]. The RNA-seq data generated in this study are available on Gene Expression Omnibus.

Single-cell RNA sequencing data analysis

The data sets (GSE135893) were downloaded from Gene Expression Omnibus (GEO) public repository[22,41]. The downloaded data were read and transformed into annotated data (anndata python package version 0.10.5, 10.1101/.12.202116.473007). In order to facilitate the downstream analysis, each category's cells (control vs. IPF) were randomly selected and the cell numbers were aligned similarly. The data were processed with standard procedure, recommended by scanpy, a scalable toolkit for analyzing single-cell gene expression data (version 1.9.8, Genome Biol 19, 15 (2018)). After cell filtering, latent space embeddings obtained with single-cell variational inference (scVI, version 0.14.6) were used for minimizing the batch effects. Subsequently, each group data were underwent the same standard normalization, dimensionality reduction, and cell type assignment. A marker specific for epithelial cells (EPCAM+) were used to assign the cell type. Scanpy core plotting functions and seaborn package (https://doi.org/10.21105/joss.03021, version 0.12.2) were used for graphical presentation. Gene expression counts were not normally distributed, therefore non-parametric statistical comparisons, Mann-Whitney U test, were performed and *p*-value were denoted in the graph.

Statistics and reproducibility

The data were presented as means ± standard deviations (SDs) or standard errors of the mean (SEMs). To assess differences between two groups, an unpaired Student's t-test was applied, while one-way ANOVA followed by Tukey's multiple comparisons test was utilized

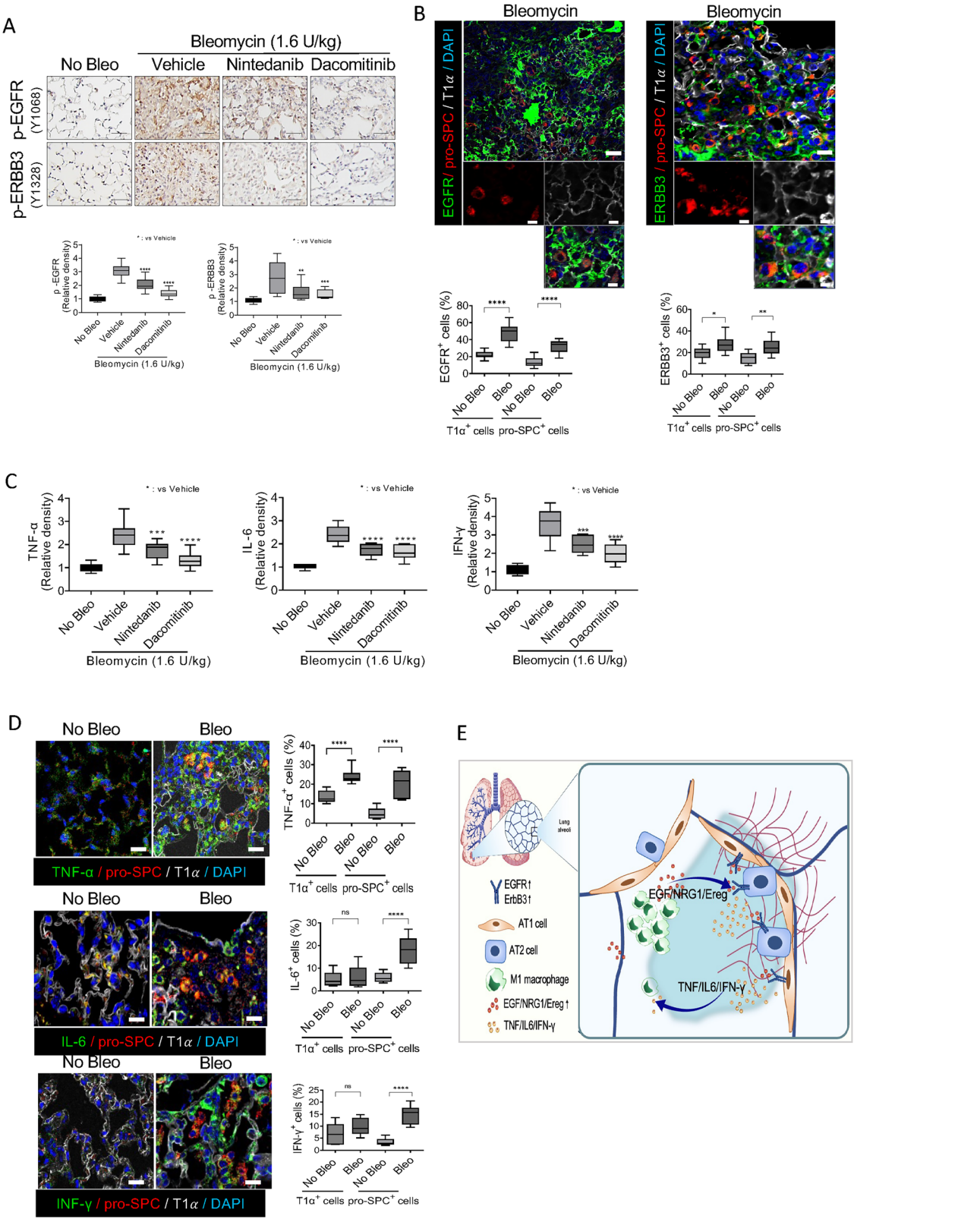

for comparisons involving more than two groups. Statistical significance was considered at p-values < 0.05. GraphPad Prism version 7.0 was used for statistical analysis. The experimenters conducting the study were blinded to group assignments and outcome assessments. Data and image analysis and plotting were performed using Image J 1.49v (NIH), R 4.0.4, Zen 3.2 (Zeiss), and Diva 7.0 (BD Biosciences). All experimental data shown are representative of at least three independent experiments.

Fig. 7 | Dacomitinib reduces EGFR1/ERBB3 phosphorylation and TNF-α, INF-γ, and IL-6 expression in alveolar epithelial cells. A Immunohistochemical detection of p-EGFR and p-ERBB3 in lung tissues from C57BL/6 mice 4 weeks after bleomycin injection treated with or without dacomitinib and nintedanib. Scale bar = 20 μm. The average of five fields of p-EGFR and p-ERBB3 density was quantified (magnification; 200×). **B** Immunofluorescence staining of EGFR (green), ERBB3 (green), pro-SPC (red), and T1α (white) was performed on lung tissues following bleomycin administration; scale bar = 10 μm; scale bar of cropped images = 5 μm. The graphs show EGFR-positive cells among T1α- and pro-SPC-positive cell populations and ERBB3-positive cells among T1α- and pro-SPC-positive cell populations. **C** Immunohistochemical detection of TNF-α, IL-6, and IFN-γ in lung tissues from C57BL/6 mice 4 weeks after bleomycin injection treated with or without dacomitinib and nintedanib; scale bar = 20 μm. The average of five fields of TNF-α, IL-6, and IFN-γ density was quantified (magnification; 200×). The graphs show the relative density of TNF-α, IL-6, and IFN-γ, respectively. **D** Immunofluorescence staining of TNF-α, IL-6, and IFN-γ (green), pro-SPC (red), and T1α (white) was performed on lung tissues treated with or without bleomycin injection; scale bar = 10 μm. The graphs show TNF-α-positive cells among T1α- and pro-SPC-positive cells, IL-6-positive cells among T1α- and pro-SPC-positive cells, and IFN-γ-positive cells among T1α- and pro-SPC-positive cells. In the graphs, the error bars indicate SEM. $^{**}P < 0.01$, $^{***}P < 0.001$ and $^{****}P < 0.0001$; ns: not significant (one-way ANOVA for multiple comparison). **E** Scheme for the Crosstalk between Pro-inflammatory Macrophages and Alveolar Epithelial Cells in Pulmonary Fibrosis Progression. Statistical significance was determined by one-way ANOVA with multiple comparisons ($^{*}P < 0.05$, $^{**}P < 0.01$, $^{***}P < 0.001$, $^{****}P < 0.0001$; ns, not significant).

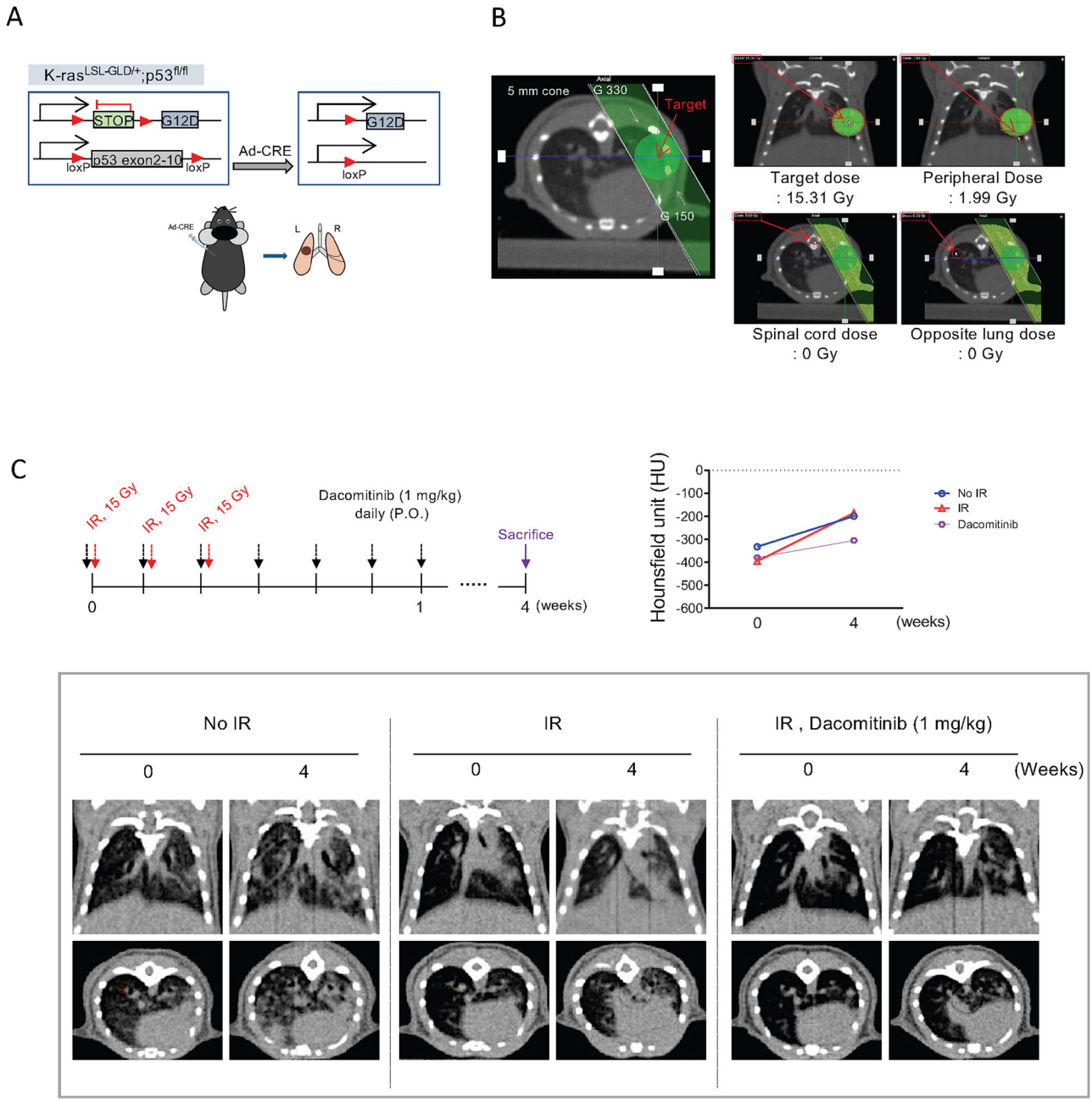

Fig. 8 | EGFR TKIs inhibit RIPF and delay tumor growth in IGRT for single-nodule NSCLC. A Schematic diagram of the local lung adenocarcinoma model. The left lung of LSL-Kras^{G12D};Trp53$^{flox/flox}$ mice was locally intrathoracically injected with Ad-CRE virus to induce single-nodule primary lung adenocarcinoma. **B** Micro-CT images of the entire thorax in LSL-Kras^{G12D};Trp53 $^{flox/flox}$ mice that received focal irradiation (IR), treated with or without dacomitinib (1 mg/kg). At 2 weeks after Ad-Cre administration, horizontal (upper), transaxial (middle), (**C**) and 3D micro-CT (bottom) images were acquired from nonirradiated animals (0 weeks) and those after focal irradiation (4 weeks). Under precise addition, normal lung volume after IGRT was greater after combined treatment with dacomitinib than that treated with vehicle. The graphs show Hounsfield units (HU) in each group.

Data availability

All data are available in the main text or the supplementary materials. Source data for the graphs can be found in Supplementary data 1. Unprocessed gels/blot can be found in Supplementary information. All other data are available from the corresponding author on reasonable request. RNA sequencing data have been deposited in the GEO repository under accession numbers GSE306230 and GSE306184.

Received: 31 January 2025; Accepted: 24 September 2025;
Published online: 01 December 2025

References

1. Shenderov, K., Collins, S. L., Powell, J. D. & Horton, M. R. Immune dysregulation as a driver of idiopathic pulmonary fibrosis. *J. Clin. Invest.* **131**, e143226 (2021).
2. Wolters, P. J. et al. Time for a change: is idiopathic pulmonary fibrosis still idiopathic and only fibrotic?. *Lancet Respir. Med.* **6**, 154–160 (2018).
3. Maher, T. M. et al. Global incidence and prevalence of idiopathic pulmonary fibrosis. *Respir. Res.* **22**, 197 (2021).
4. Wynn, T. A. & Ramalingam, T. R. Mechanisms of fibrosis: therapeutic translation for fibrotic disease. *Nat. Med.* **18**, 1028–1040 (2012).
5. Grimminger, F., Gunther, A. & Vancheri, C. The role of tyrosine kinases in the pathogenesis of idiopathic pulmonary fibrosis. *Eur. Respir. J.* **45**, 1426–1433 (2015).
6. Pakshir, P. & Hinz, B. The big five in fibrosis: Macrophages, myofibroblasts, matrix, mechanics, and miscommunication. *Matrix Biol.* **68-69**, 81–93 (2018).
7. Prasse, A. et al. A vicious circle of alveolar macrophages and fibroblasts perpetuates pulmonary fibrosis via CCL18. *Am. J. Respir. Crit. Care Med.* **173**, 781–792 (2006).
8. Lierova, A. et al. Cytokines and radiation-induced pulmonary injuries. *J. Radiat. Res.* **59**, 709–753 (2018).
9. Chen, Y. et al. Circulating IL-6 as a predictor of radiation pneumonitis. *Int. J. Radiat. Oncol. Biol. Phys.* **49**, 641–648 (2001).
10. Yara, S. et al. FTS reduces bleomycin-induced cytokine and chemokine production and inhibits pulmonary fibrosis in mice. *Clin. Exp. Immunol.* **124**, 77–85 (2001).
11. Piguet, P. F., Collart, M. A., Grau, G. E., Kapanci, Y. & Vassalli, P. Tumor necrosis factor/cachectin plays a key role in bleomycin-induced pneumopathy and fibrosis. *J. Exp. Med.* **170**, 655–663 (1989).
12. Phan, S. H. & Kunkel, S. L. Lung cytokine production in bleomycin-induced pulmonary fibrosis. *Exp. Lung Res.* **18**, 29–43 (1992).
13. Everson, M. P. & Chandler, D. B. Changes in distribution, morphology, and tumor necrosis factor-alpha secretion of alveolar macrophage subpopulations during the development of bleomycin-induced pulmonary fibrosis. *Am. J. Pathol.* **140**, 503–512 (1992).
14. Vallath, S., Hynds, R. E., Succony, L., Janes, S. M. & Giangreco, A. Targeting EGFR signalling in chronic lung disease: therapeutic challenges and opportunities. *Eur. Respir. J.* **44**, 513–522 (2014).
15. Aegerter, H., Lambrecht, B. N. & Jakubzick, C. V. Biology of lung macrophages in health and disease. *Immunity* **55**, 1564–1580 (2022).
16. Odell, I. D. et al. Epiregulin is a dendritic cell-derived EGFR ligand that maintains skin and lung fibrosis. *Sci. Immunol.* **7**, eabq6691 (2022).
17. Epstein Shochet, G., Brook, E., Eyal, O., Edelstein, E. & Shitrit, D. Epidermal growth factor receptor paracrine upregulation in idiopathic pulmonary fibrosis fibroblasts is blocked by nintedanib. *Am. J. Physiol. Lung Cell Mol. Physiol.* **316**, L1025–L1034 (2019).
18. Chen, L., Fu, W., Zheng, L., Liu, Z. & Liang, G. Recent progress of small-molecule epidermal growth factor receptor (EGFR) inhibitors against C797S resistance in non-small-cell lung cancer. *J. Med. Chem.* **61**, 4290–4300 (2018).
19. Zhang, L. et al. Macrophages: friend or foe in idiopathic pulmonary fibrosis?. *Respir. Res.* **19**, 170 (2018).
20. Misharin, A. V. et al. Monocyte-derived alveolar macrophages drive lung fibrosis and persist in the lung over the life span. *J. Exp. Med.* **214**, 2387–2404 (2017).
21. Habermann, A. C. et al. Single-cell RNA sequencing reveals profibrotic roles of distinct epithelial and mesenchymal lineages in pulmonary fibrosis. *Sci. Adv.* **6**, eaba1972 (2020).
22. Adams, T. S. et al. Single-cell RNA-seq reveals ectopic and aberrant lung-resident cell populations in idiopathic pulmonary fibrosis. *Sci. Adv.* **6**, eaba1983 (2020).
23. Nava, M. et al. Transcriptomic and ChIP-sequence interrogation of EGFR signaling in HER2+ breast cancer cells reveals a dynamic chromatin landscape and S100 genes as targets. *BMC Med. Genomics* **12**, 32 (2019).
24. Cho, J. et al. High dose-per-fraction irradiation of limited lung volumes using an image-guided, highly focused irradiator: simulating stereotactic body radiotherapy regimens in a small-animal model. *Int. J. Radiat. Oncol. Biol. Phys.* **77**, 895–902 (2010).
25. Choi, S. H. et al. A hypoxia-induced vascular endothelial-to-mesenchymal transition in development of radiation-induced pulmonary fibrosis. *Clin. Cancer Res.* **21**, 3716–3726 (2015).
26. Jin, H. et al. Radiation-induced lung fibrosis: preclinical animal models and therapeutic strategies. *Cancers* **12**, 1561 (2020).
27. Hong, Z. Y. et al. Time, dose, and volume responses in a mouse pulmonary injury model following ablative irradiation. *Lung* **194**, 81–90 (2016).
28. Engelman, J. A. et al. PF00299804, an irreversible pan-ERBB inhibitor, is effective in lung cancer models with EGFR and ERBB2 mutations that are resistant to gefitinib. *Cancer Res.* **67**, 11924–11932 (2007).
29. Gonzales, A. J. et al. Antitumor activity and pharmacokinetic properties of PF-00299804, a second-generation irreversible pan-erbB receptor tyrosine kinase inhibitor. *Mol. Cancer Ther.* **7**, 1880–1889 (2008).
30. Li, D. et al. BIBW2992, an irreversible EGFR/HER2 inhibitor highly effective in preclinical lung cancer models. *Oncogene* **27**, 4702–4711 (2008).
31. Propper, D. J. et al. PANTHER: AZD8931, inhibitor of EGFR, ERBB2 and ERBB3 signalling, combined with FOLFIRI: a Phase I/II study to determine the importance of schedule and activity in colorectal cancer. *Br. J. Cancer* **128**, 245–254 (2023).
32. Oda, K., Matsuoka, Y., Funahashi, A. & Kitano, H. A comprehensive pathway map of epidermal growth factor receptor signaling. *Mol. Syst. Biol*. **1**, 2005-0010 (2005).
33. Song, Y. et al. Identification of radiation-induced EndMT inhibitors through cell-based phenomic screening. *FEBS Open Bio* **9**, 82–91 (2019).
34. Hill, C. et al. Autophagy inhibition-mediated epithelial-mesenchymal transition augments local myofibroblast differentiation in pulmonary fibrosis. *Cell Death Dis.* **10**, 591 (2019).
35. Hong, Z. Y., Song, K. H., Yoon, J. H., Cho, J. & Story, M. D. An experimental model-based exploration of cytokines in ablative radiation-induced lung injury in vivo and in vitro. *Lung* **193**, 409–419 (2015).
36. Merad, M. & Martin, J. C. Pathological inflammation in patients with COVID-19: a key role for monocytes and macrophages. *Nat. Rev. Immunol.* **20**, 355–362 (2020).
37. Fajgenbaum, D. C. & June, C. H. Cytokine Storm. *N. Engl. J. Med.* **383**, 2255–2273 (2020).
38. Hutchinson, J., Fogarty, A., Hubbard, R. & McKeever, T. Global incidence and mortality of idiopathic pulmonary fibrosis: a systematic review. *Eur. Respir. J.* **46**, 795–806 (2015).
39. Finnerty, J. P., Ponnuswamy, A., Dutta, P., Abdelaziz, A. & Kamil, H. Efficacy of antifibrotic drugs, nintedanib and pirfenidone, in treatment of progressive pulmonary fibrosis in both idiopathic pulmonary fibrosis (IPF) and non-IPF: a systematic review and meta-analysis. *BMC Pulm. Med.* **21**, 411 (2021).

40. Simeon, S., Jongkon, N., Chotpatiwetchkul, W. & Gleeson, M. P. Insights into the EGFR SAR of N-phenylquinazolin-4-amine-derivatives using quantum mechanical pairwise-interaction energies. *J. Comput. Aided Mol. Des.* **33**, 745–757 (2019).
41. Colomba, A. et al. Targeting the HER3 pseudokinase domain with small molecule inhibitors. *Methods Enzymol.* **667**, 455–505 (2022).
42. Tisoncik, J. R. et al. Into the eye of the cytokine storm. *Microbiol. Mol. Biol. Rev.* **76**, 16–32 (2012).
43. She, Y. X., Yu, Q. Y. & Tang, X. X. Role of interleukins in the pathogenesis of pulmonary fibrosis. *Cell Death Discov.* **7**, 52 (2021).
44. Borthwick, L. A., Wynn, T. A. & Fisher, A. J. Cytokine mediated tissue fibrosis. *Biochim. Biophys. Acta* **1832**, 1049–1060 (2013).
45. Rosen, I. I. et al. Correlation between lung fibrosis and radiation therapy dose after concurrent radiation therapy and chemotherapy for limited small cell lung cancer. *Radiology* **221**, 614–622 (2001).
46. Liu, L. et al. Epithelial-mesenchymal transition in organ fibrosis development: current understanding and treatment strategies. *Burns Trauma* **10**, tkac011 (2022).
47. Nam, J. K. et al. Pharmacologic inhibition of HIF-1alpha attenuates radiation-induced pulmonary fibrosis in a preclinical image guided radiation therapy. *Int. J. Radiat. Oncol. Biol. Phys.* **109**, 553–566 (2021).
48. Rynikova, M. et al. Transcriptomic analysis of macrophage polarization protocols: vitamin D(3) or IL-4 and IL-13 do not polarize THP-1 monocytes into reliable M2 macrophages. *Biomedicines* **11**, 608 (2023).
49. Tan, Q., Choi, K. M., Sicard, D. & Tschumperlin, D. J. Human airway organoid engineering as a step toward lung regeneration and disease modeling. *Biomaterials* **113**, 118–132 (2017).
50. Trapnell, C. et al. Differential gene and transcript expression analysis of RNA-seq experiments with TopHat and Cufflinks. *Nat. Protoc.* **7**, 562–578 (2012).
51. Shannon, P. et al. Cytoscape: a software environment for integrated models of biomolecular interaction networks. *Genome Res.* **13**, 2498–2504 (2003).
52. Naba, A. et al. The matrisome: in silico definition and in vivo characterization by proteomics of normal and tumor extracellular matrices. *Mol. Cell Proteom.* **11**, M111.014647 (2012).
53. Du, Y., Guo, M., Whitsett, J. A. & Xu, Y. 'LungGENS': a web-based tool for mapping single-cell gene expression in the developing lung. *Thorax* **70**, 1092–1094 (2015).
54. Du, Y. et al. Lung Gene Expression Analysis (LGEA): an integrative web portal for comprehensive gene expression data analysis in lung development. *Thorax* **72**, 481–484 (2017).
55. Subramanian, A. et al. Gene set enrichment analysis: a knowledge-based approach for interpreting genome-wide expression profiles. *Proc. Natl Acad. Sci. USA* **102**, 15545–15550 (2005).
56. Yu, G., Wang, L. G., Han, Y. & He, Q. Y. clusterProfiler: an R package for comparing biological themes among gene clusters. *OMICS* **16**, 284–287 (2012).
57. Robinson, M. D., McCarthy, D. J. & Smyth, G. K. edgeR: a Bioconductor package for differential expression analysis of digital gene expression data. *Bioinformatics* **26**, 139–140 (2010).
58. Dolgalev, I. & Tikhonova, A. N. Connecting the dots: resolving the bone marrow niche heterogeneity. *Front. Cell Dev. Biol.* **9**, 622519 (2021).
59. Gu, Z., Eils, R. & Schlesner, M. Complex heatmaps reveal patterns and correlations in multidimensional genomic data. *Bioinformatics* **32**, 2847–2849 (2016).

Acknowledgements

This project was funded by the following sources: the National Research Foundation (NRF-2020M2D9A2093964), supported by the Ministry of Science and ICT (MSIT), Republic of Korea, the National Research Foundation under MSIT (RS-2023-NR077180, RS-2022-NR069239 and RS-2024-00398073) and the Korea Institute of Radiological & Medical Sciences, MIST (KIRAMS, 50531-2025).

Author contributions

Y.J.L. conceived and designed the study. J.H.K., S.H.C., J.K.N., and M.S.P. performed the experiments with help from H.J.L., J.C., and H.R.S. I.C. contributed to data analysis. S.H.C. and J.L. provided support for bioinformatic analysis. Y.J.L., S.H.C., and J.H.K. drafted the manuscript.

Competing interests

The authors declare no competing interests.

Additional information

Supplementary information The online version contains supplementary material available at https://doi.org/10.1038/s42003-025-08940-w.

Correspondence and requests for materials should be addressed to Yoon-Jin Lee.

Peer review information *Communications Biology* thanks the anonymous reviewers for their contribution to the peer review of this work. Primary Handling Editor: Joao Valente. A peer review file is available.